SAPIENZA
UNIVERSITÀ DI ROMA

Correlation between High Energy Cosmic Rays Observed by Auger and Telescope Array and Detected Neutrinos from the Telescope ANTARES

Facoltà di Scienze Matematiche, Fisiche e Naturali

Corso di Laurea Magistrale in Astronomia e Astrofisica

Candidate

Giovanni Renzi

ID number 1462349

Thesis Advisor

Prof. Antonio Capone

Co-Advisor

Dr. Irene Di Palma

Academic Year 2015-16

Correlation between High Energy Cosmic Rays Observed by Auger and Telescope Array and Detected Neutrinos from the Telescope ANTARES
Master thesis. Sapienza – University of Rome

This thesis has been typeset by LaTeX and the Sapthesis class.

Author's email: gio.renzi92@gmail.com

Alla mia famiglia

Tutto posso in colui che mi dà la forza
Fil 4,13

Contents

Introduction

Since the Hess Balloon experiment in 1912, the study of Cosmic Rays has interested many physicists for different scopes, and in particular the study of the nature of these particles had involved during the years balloon, space and ground experiments.

In the last years the study of Cosmic Rays has developed greatly, principally due to the improvement of techniques of detection. This fact allows to investigate at increasingly high energy and to measure not only sign, mass and energy of a particle but also its incoming direction. Great surface experiments such as Pierre Auger Observatory(PAO) and Telescope Array (TA), using many different techniques such as Cherenkov tanks, air Cherenkov telescopes, fluorescence detectors, scintillators and others, can measure the angular direction in the sky of Cosmic Rays with a precision of few degrees. Other experiments such as ANTARES and IceCube, great cubes of water (liquid or ice), want to recognize and map astrophysical neutrinos through the detection of secondary leptons (e, μ or τ) in charged current interactions or through the detection of neutral current interaction products.

In the last years there has made great use of multimessenger approach in analysing data: different kinds of experiments collaborate to improve the capability and sensitivity of detection of each one and to find common results. For example real time warnings of detections can indicate a reduced field of search for other experiments to focus on, or searching for correlations between data from different experiments can improve the discovery potential in the search for sources of events.

The aim of this thesis is to use public data of Cosmic Ray detections from Auger and TA databases and of neutrinos from ANTARES to search a correlation between them that could indicate the existence of common sources in a multimessenger approach. We want to consider also the effect of galactic and extragalactic magnetic fields. Regarding the first, we based our simulations on a determined model of the galactic field. Then we built a simple example of extragalactic magnetic field in which particles can propagate. Such work allowed us to study the correlation just written, building a statistical test including simulations of background distribution for comparison with data.

We report the work done for this thesis as follows. In the first chapter cosmic rays are presented in an overview on many aspects; in the same chapter neutrinos are introduced too. The second chapter is written about the experiments involved in this thesis and their main characteristic. The third chapter is on the multimessenger astronomy, describing different kind of approaches and a few examples of multimessenger analyses. The fourth chapter treats of simulations done with the software CrPropa to evaluate the deflection due to galactic and extra-galactic magnetic fields on the cosmic rays. The fifth chapter displays data used for the search

of correlation and presents the analysis proceedings adopted to do this. In the sixth chapter results obtained in the study of correlation are showed and commented.

Chapter 1

Cosmic Rays

In this first chapter the status of art of cosmic ray is presented. After a historical and scientific preview, energy spectrum is introduced, then interaction of charged particles with magnetic fields is discussed. Afterwards techniques for detecting increasing energy cosmic rays are showed and then the present open questions about cosmic rays are shown. In the end a view of neutrino characteristics and detection techniques is done.

1.1 A first look

In 1912 Victor Hess flew on a balloon to measure radiation in function of the height and observed that it increased with the height and so it can't be of terrestrial origin but that particles was coming from space. In 1925 Robert Millikan conceived the name "cosmic rays". Then Arthur Compton theorized that this radiation was charged particles and in 1933, from the idea of Bruno Rossi to observe the behaviour of cosmic rays in the earth magnetic field, Compton made out that they were charged particles.

Primary cosmic rays are particles of galactic and extragalactic origin that reach the Earth and interact with atmosphere atoms causing showers of particles (secondary cosmic rays). There are electro-magnetic and hadronic particles that generate different kinds of showers. The first ones are less wide and are composed principally of electrons and photons. The second ones have a greater width and are characterized by the presence of hadronic particles and long tracking muons.

In 1990s cosmic rays were observed with balloon experiments in high atmosphere like IMAX, MASS, HEAT and BESS. The aim of these experiments was to detect antimatter particles and find the antimatter-to-matter ratio. This was done with instruments like Ring Imaging Cherenkov detectors, Time of Flight detectors, Transition Radiation detectors, trackers and calorimeters to measure mass, charge and sign of the charge of particles.

After 2000 cosmic rays detectors like PAMELA and the Alpha Magnetic Spectrometer were sent in the space to improve the ability of detecting primary particles. Meanwhile the study of the development of showers in the atmosphere brought to build experiments at high altitude to measure more energetics showers. There were detectors to measure photons like ARGO and MILAGRO and hadronic showers

detectors like KASCADE-Grande, EAS-Top, Casa-MIA. Then there was the development of Hybrid detectors to detect ultra high energy air extensive showers such as AGASA and HiRes and then for extremely high energy showers the Pierre Auger Observatory and the Telescope Array (TA).

The first approach to neutrino astronomy was for the study of solar neutrinos produced in the *p-p* chain. Since the beginning experiments like Homestake Mine, then GALLEX/GNO, SAGE, Kamiokande, and later Super Kamiokande, measured a lack in the observed flux of electron neutrinos (ν_e) from the Sun with respect to the expected one. This lack, as confirmed recently by SNO, is due to neutrino oscillation, so 2/3 of the ν_e flux change their flavour, hence having their energy under the threshold for their detection. A very important step towards neutrino astronomy was the detection of about 20 neutrinos from the famous Supernova 1987A. In the last half century it was born the idea to detect neutrinos in large natural water volumes and so it has been developed a method to indirectly detect primary neutrinos in such places with a grid of detectors placed in the volume through long strings linked to the shore by optical fiber cables. The first try to put detectors under the sea was done by the experiment DUMAND, but they did not have great results, nonetheless it was an important experience for the develop of technologies able to survive to strong pressure and send data to the shore. The first to arrange a real neutrino telescope was the Baikal Neutrino Observatory, still active since 1995 and a pioneer for all following experiments for its important studies about water properties. The first experiment to develop in the ice was AMANDA. Today experiments occupy large volumes of iced (IceCube) or liquid (ANTARES) water and there are projects to improve all the telescopes with KM3Net in the Mediterranean Sea and the enlargement of IceCube and Baikal.

1.2 Energy spectrum

It is very important to study the flux of cosmic rays in function of the energy to understand their mass composition and the processes that can accelerate them. The observed cosmic rays energy spectrum has a quasi-linear trend in which most of its sections follow a power-law[1] of the form:

$$\frac{dN}{dE} = K \cdot E^{-\alpha} \tag{1.1}$$

The index α has a value of 2.7 up to about 10^{15} eV where there is the so-called "knee" in which the index changes and becomes 3.1 till about 10^{19} eV where there is the "ankle" and the spectrum flattens again to an α value of 2.7. Up to the knee measures show that the cosmic rays are mainly protons (90%) with a little part of heavier nuclei (9% helium and 1% heavier nuclei). The steepening of the spectrum at the knee is probably due to an increase of the average mass of the nuclei.

The change of slope at the ankle takes to the thought that a new injection of protons inserts in the count of cosmic rays, and that these particles, because protons with such an energy are not contained in the Galaxy as shown by the formula for the gyroradius (1.2), are thought to be of extragalactic origin. However different

[1] Most of the general notions are from [1]

measures taken by many experiments (in particular Auger and Telescope Array) still leaves great doubts about the real composition of the cosmic rays in this region of the spectrum as it will be discussed in section 1.6.

$$R[\text{kpc}] = 10 \cdot \frac{E[\text{Eev}]}{ZB[\mu\text{G}]} \tag{1.2}$$

Figure 1.1. All particles energy spectrum [2].

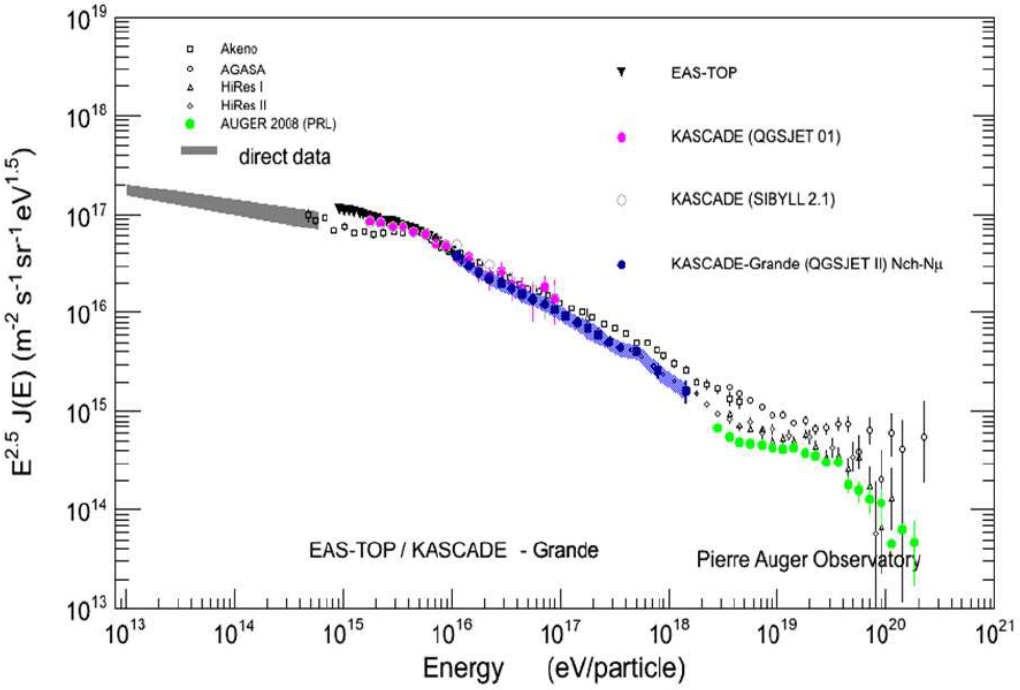

The index 2.7 is well described considering the first order Fermi acceleration mechanism and the escape time from the Galaxy in the so-called "leaky box model". This means treating for example the Milky Way as a homogeneous box, in which cosmic rays propagate until they lose their energy or escape. From the leaky box model, considering hence a homogeneous space, stationarity and neglecting interactions (we can do this because the time for interacting is a order of magnitude higher than the escape time) we have:

$$\frac{dN}{dE} \simeq Q_E \cdot \tau_{esc} \tag{1.3}$$

where Q_E is the flux from sources and τ_{esc} the time of escape from the Galaxy. The first order Fermi acceleration mechanism (par. 1.2.1) gives a flux from the sources of $Q_E \sim E^{-(2\div 2.2)}$. Measures from the spallation processes (par. 1.2.2) give a time of escape from the Galaxy following the law $\tau_{esc} \sim E^{-(0.6\div 0.7)}$, so we have $\frac{dN}{dE} \simeq Q_E \cdot \tau_{esc} \sim E^{-2.7}$ in agreement with the observations.

1.2.1 First order Fermi acceleration mechanism

First order Fermi acceleration mechanism [1] calculate the energy gain of gas particles interacting with a shock front. The shock front has a velocity $-u_1$ and the gas has a velocity relative to the front u_2. In the rest frame the gas has velocity $V = -u_1 + u_2$. In the gas frame, a particle has energy

$$E_1^* = \gamma E_1(1 - \beta \cos\theta_1) \tag{1.4}$$

where γ and β are respectively Lorentz factor and boost of the gas, that is $\beta = (u_1 - u_2)/c$, and θ_1 the entering angle of the particle respect to the gas velocity; the $*$ indicates the gas frame. When a particle is coming out of the gas, it has energy

$$E_2 = \gamma E_2^*(1 + \beta \cos(\theta_2^*)) \tag{1.5}$$

where θ_2^* is the exiting angle of the particle respect to the gas velocity. Considering that the particle in the gas is only affected by magnetic field, we can write $E_1^* = E_2^*$, hence

$$\frac{\Delta E}{E} = \frac{1 - \beta\cos\theta_1 + \beta\cos\theta_2^* - \beta^2\cos\theta_1\cos\theta_2^*}{1 - \beta^2} - 1 \tag{1.6}$$

To calculate $< \cos\theta_1 >$ and $< \cos\theta_2^* >$ we need he probability of a particle to affect the shock, that is $\frac{dP}{d\Omega} \propto \frac{v}{c}\cos\theta$. Integration extremes are $0 \leq cos\theta_2^* \leq 1$ and $-1 \leq \cos\theta_1 \leq 0$. Considering that for a generic θ is

$$<\cos\theta> = \frac{\int \cos\theta \frac{dP}{d\Omega} d\Omega}{\int \frac{dP}{d\Omega} d\Omega} \tag{1.7}$$

we have $<\cos\theta_1> = -\frac{2}{3}$ and $<\cos\theta_2^*> = \frac{2}{3}$ and then

$$\frac{<\Delta E>}{<E>} = \frac{4}{3}\beta \tag{1.8}$$

This kind of mechanism has a power-law energy spectrum. In fact, calling l the mean free path of a particle, the frequency of interaction can be defined such as

$$f_I = \frac{V + u_1}{l} \tag{1.9}$$

From this, assuming $u_1 \sim c$, it can be written

$$\frac{\Delta E}{\Delta t} = \frac{4}{3} \cdot \frac{V + u_1}{l} \cdot \frac{V}{c} \cdot E \simeq \frac{4}{3}\frac{V}{l}E = \frac{E}{\tau_F} \tag{1.10}$$

from which, calling $\frac{t}{\tau_F} = \alpha$

$$E = C \cdot E^{-\alpha} \tag{1.11}$$

The energy spectrum index from this mechanism is $\alpha = -(2 \div 2.2)$.

1.2.2 Spallation processes

Spallation processes are responsible for the presence of some nuclei in the Galaxy. A classic example is the spallation of Carbon to produce Boron, that otherwise it would not be produced in any way.
A generic spallation process can be written as

$$p + A \rightarrow B \tag{1.12}$$

and from the leaky box model (this time we have no flux from sources, but we have to consider interactions) we have

$$\frac{N_B(E)}{N_A(E)} = BR(A \rightarrow B) \cdot \tau_{esc}^B(E) \cdot \frac{c}{\lambda_{int}} = BR(A \rightarrow B) \cdot \tau_{esc}^B(E) \cdot c \cdot \sigma_{int}^A \cdot < n_{ISM} > \tag{1.13}$$

where $BR(A \rightarrow B)$ is the branching ratio of the process and λ_{int} is the interaction length, expressed in the second step in function of A cross section for interactions σ_{int}^A and numerical density of interstellar medium $<n_{\rm ISM}>$. Hence, from measures of spallation products, τ_{esc} can be get and

$$\tau_{esc}(E) \sim E^{-(0.6 \div 0.7)} \tag{1.14}$$

1.3 Interaction with magnetic field

Since cosmic rays are mainly charged particles their propagation is influenced by the presence of magnetic field, as Lorentz force shows:

$$F_L = q\vec{v} \times \vec{B} \tag{1.15}$$

The acceleration due to this force is perpendicular to travelling particles, so it only deflects particle trajectories, not changing module of velocity. This considerations bring to not neglect the presence of magnetic fields in the galactic and intergalactic mediums.
In the following it will be shown a summary of the knowledge about galactic and extragalactic magnetic fields.

1.3.1 Galactic magnetic field

The Milky Way is a barred spiral galaxy of radius $\sim 15 \div 20$kpc (the halo is much larger) and thickness of the stellar disk $\sim 0.6\,$kpc, its age is $\geq 13.7\,$Gyrs and contains a mass of $\sim 10^{12}_{\odot}$. The Galaxy has four main spiral arms and at least two smaller arms. The Sun is at $\sim 8\,$kpc from the galactic centre in the Orion-Cygnus Arm.

Study of galactic magnetic field is greatly limited by the difficult to interpret data and mostly by the fact that we are in the Galaxy itself. However we have information about magnetic field from measures of synchrotron radiation and Faraday rotation [3] and we know that the field is of the order of μG. In our galaxy there are both coherent and random components and from observations it is known that in other galaxies magnetic field tends to follow the spiral structure of the gas and stellar

population. There are also non-coherent components and it is thought that there are two of these, an isotropic one, probably turbulent, contributing only to the average total intensity, and a "striated" one, contributes to polarization, which is sensitive to orientation. Northern hemisphere seems to have a lower magnetic field intensity than Southern hemisphere. Many models have been taking into account for the galactic magnetic field and one of the most appreciated at present time is the so-called JF12 model by Jansson and Farrar [4], that we will use for this work and it is schematized in fig. 1.2 and 1.3.

Figure 1.2. Top view of slices in $x-y$ plane of Galaxy magnetic field of JF12 model. *Top.* From left slices at $z = 10\,\mathrm{pc}$ and $z = -10\,\mathrm{pc}$. *Bottom.* From left slice at $z = 1\,\mathrm{kpc}$ and $z = -1\,\mathrm{kpc}$.

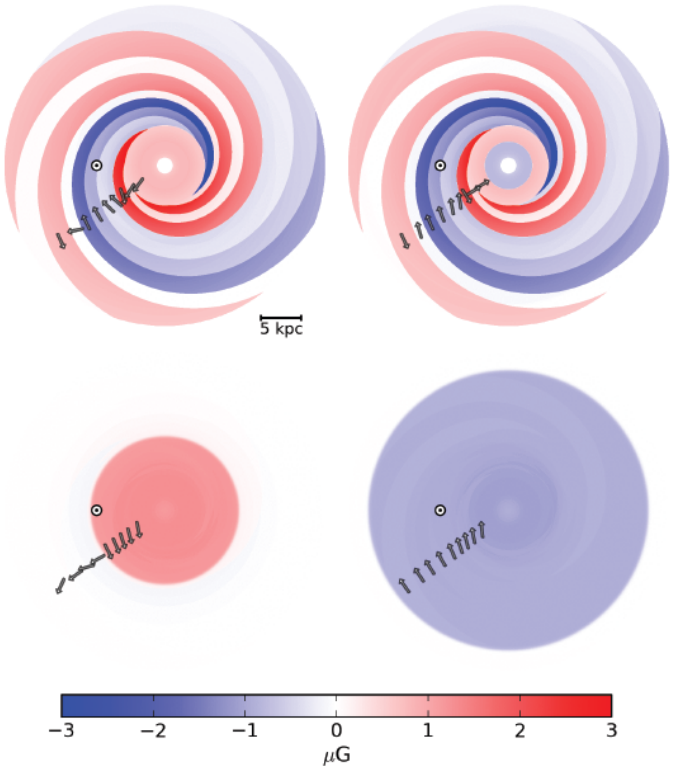

1.3.2 Extragalactic magnetic field

Extragalactic magnetic field is even less known than the galactic one. Magnetic field of single objects like globular clusters and galaxies are known, but the strength of a diffuse intergalactic magnetic field is currently poorly known, both for the difficult of measures and their interpreting. Recent studies [5] put upper limits on the average field of the order of 1 nG.

Figure 1.3. Slice on the $x - z$ plane of JF12 model.

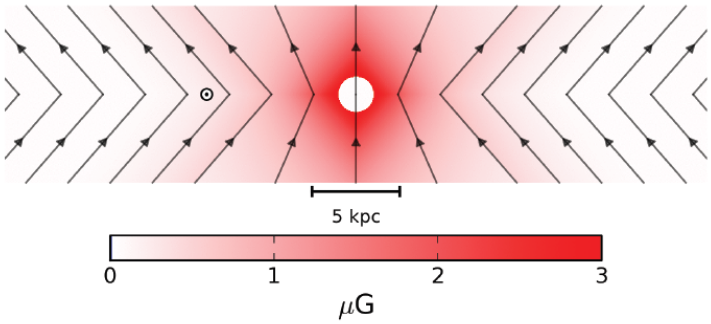

1.4 Extensive air showers

The shape of showers of secondary particles in the atmosphere is strongly dependent on energy and nature of the primary cosmic rays producing them. The basic interactions for a shower generated from a proton are

$$p + N \rightarrow \pi^{\pm}, \pi^{0}, K^{\pm}, K^{0}, p, n, \ldots \tag{1.16}$$

Short-lived hadrons decay in cascades of photons, electrons and positrons (electromagnetic component) and muons and neutrinos (penetrating component).
Primary particles with high energy generate the so-called "extensive air showers". The choice to detect this type of particles at the ground brought to the necessity of study the develop of such particle cascades.

The simplest model possible to reproduce a shower is imaging that every particle with energy E_0, when interacting, "splits" in more particles with a fraction $f \cdot E_0$ of the energy each one. This happen depending on the probability of interaction. Length of interaction $\lambda_{int} = \frac{1}{n\sigma}$ is defined as the path a particle can travel on average before interacting. n is the numerical density of the medium crossed, σ is the cross section. So after t steps the mean energy of the particles of the shower will be $f^t \cdot E$, and the path travelled, called depth, will be $X = t \cdot \lambda_{int}$. It is known that energy losses at high energy are dominated by coulombian process while at low energy they are dominated by ionization. Decreasing energy, the point at which ionization become more important, called critical energy (E_c), is reached. After a number of steps t_{max}, it will be $E = f^{X_{max}/\lambda_{int}} E_0 = E_c$ and so $f^{-X/\lambda} = E_0/E_c$. Below this energy the number of interactions decrease till arriving at the ground, so the maximum number of particles has been reached at the depth $X_{max} = \frac{\ln(E_0/E_c)}{\ln(1/f)}$. It is clear that particles with higher energy have a higher X_{max}. This information can help recognize the nature of the primary cosmic ray incoming. For a nucleus with atomic number A, we can consider its energy as parted between all its nucleons that hence have mean energy E/A. We can also consider each nucleon interacting independently. X_{max} for heavier nuclei is hence shorter then that of lighter ones.

1.5 High energy detection techniques

In this section main detection techniques for high energy cosmic rays are presented.

1.5.1 Cherenkov effect

In a medium the speed of light is $c_m = \frac{c}{n}$ where n is the refraction index. This means that a particle with enough energy can travel in a medium with a speed that is higher than the speed of light. The passage of a particle in these conditions polarizes the near molecules generating a dipole moment. When excited molecules return to the ground state they emit photons that coherently sum on a cone surface (Cherenkov [6] cone) with characteristic angle:

$$cos\Theta_C = \frac{1}{\beta n} \tag{1.17}$$

where β is the relativistic boost of the travelling particle. The number of photons induced for path unit and wavelenght unit is

$$\frac{dN_\gamma}{dxd\lambda} = \frac{2\pi}{137\lambda^2} \cdot (1 - \frac{1}{\beta^2 n^2}) \tag{1.18}$$

Cherenkov effect can be observed in different mediums like air, with specific telescopes, or water, as in neutrino detection experiments.

1.5.2 Air Cherenkov Telescopes

The air refraction index is typically ~ 1.0003, so for a particle with boost $\beta = 0.9999$ the Cherenkov angle is $\Theta_C \simeq 20\,\text{mrad} \simeq 1.2^o$. The threshold energy for an electron is $E_e \geq 21\,\text{MeV}$ and for a muon is $E_\mu \geq 4.4\,\text{GeV}$. Considering that the maximum development of a shower is at a height of $\sim 10\,\text{km}$, the surface covered by Cherenkov light can be computed as follows: the radius is $r \simeq 10\,000\,\text{m} \cdot 0.020 = 200\,\text{m}$ so we have $A = \pi r^2 \simeq 1.6 \cdot 10^5\,\text{m}^2$. In the visible light for an electro-magnetic shower total energy of 1 TeV we expect $30 \div 50$ $photons/\text{m}^2$ on a 100 m area from the shower axis. This detection technique has a duty cycle of $(10 \div 20)\%$ because it can be active only on good weather nights in searching for sources above the horizon.

The Cherenkov light emitted in this way is a short flash of $5 \div 20$ ns for each shower and photons are collected by mirrors and focused on a fast PMTs camera where the shower is "imaged". This way of imaging the shower places the source on camera centre when the telescope is pointed on the source (fig. 1.4).

This kind of detection can distinguish the leptonic or hadronic nature of a shower knowing the different characteristic of each one.

Using stereoscopically more telescopes there is a big gain in the precision to determine the primary particle direction.

This technique is used to detect showers with energy in the range $30\,\text{GeV} \div 30\,\text{TeV}$.

1.5.3 Surface detectors

The great extension at ground of showers with energy $E >$ TeV makes very difficult to completely cover such an area with detectors, so this brought to the idea of "sampling" the showers spreading detectors on the area at a certain distance each other. Models of how a shower can be detected are done through MonteCarlo simulations and so the primary energy and the axis direction can be reconstructed.

Figure 1.4. Cherenkov imaging example. The telescope is pointed to the blue shower direction: the shower image point to the centre, the red shower image doesn't do it.

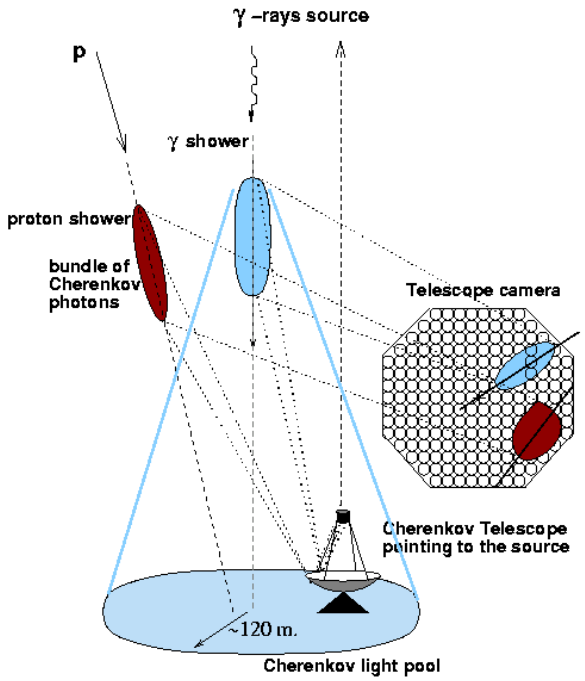

There can be different kinds of detectors to do this surface detection. One of these is building water tanks where to exploit Cherenkov effect. The energy of particles is calculated counting the number of Cherenkov photons emitted with PMTs. Another possibility is using scintillator detectors through which the light is taken to PMTs.

1.5.4 Fluorescence detectors

When a shower passes through the air, particles with ultra high energy (UHE) interact with nitrogen atoms of N_2 molecules exciting them. When the nitrogen atoms return to ground state they emit ultra-violet light in all directions. This light can be detected by Telescopes and used for example to see the plan on which showers lie (fig. 1.5). Also in this case the light is visible only on night and the duty cycle is, as for Air Cherenkov, $(10 \div 20)\%$. This technique is complementary to the surface detection and can be used to build hybrid detectors using different techniques at the same time. Fluorescence detectors are able to measure the depth at which there is X_{max}, measuring the direction from where the maximum of light comes, so this technique is also very useful to distinguish different primary particle nuclei.

Figure 1.5. Fly's Eye experiment particular example of using fluorescence detectors in addition to Cherenkov tanks.

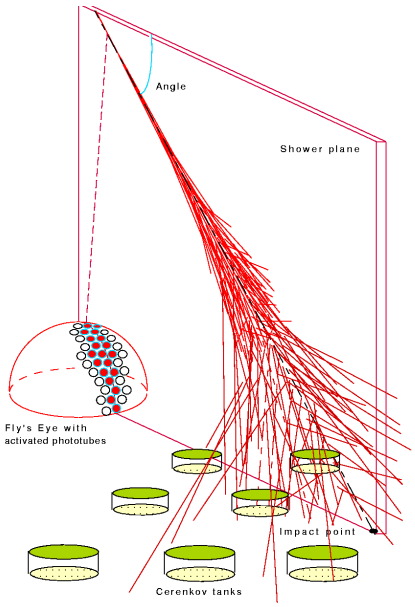

1.6 Present questions: GZK effect and the composition at very high energies

1.6.1 GZK effect

There is an important theoretical limit to the propagation of particles at energies above 10^{19} eV. As described by Greisen [7], Zatsepin and Kuzmin [8], a proton with enough energy can interact with the Cosmic Microwave Background (CMB) photons in a process represented by these two branches:

$$p + \gamma_{\mathrm{CMB}} \rightarrow \Delta^{+} \begin{array}{l} \rightarrow \pi^{0} + p \\ \rightarrow \pi^{+} + n \end{array} \tag{1.19}$$

The energy at which this effect becomes important is about

$$E_{cut-off} = 5 \cdot 10^{19}\,\mathrm{eV} \tag{1.20}$$

where there should be a cut-off. For heavier nuclei we can consider the total energy as distributed between all nucleons and so, for example, a Fe nucleus needs an energy that is 56 times greater than that needed for a single proton to interact in this way. Hence the problem of composition becomes extremely relevant when cosmic rays have higher cut-off energy than protons.

The volume in which a proton with energy in GZK range can travel without interacting is called GZK volume and it is considered to have radius of a few mega-parsecs.

1.6.2 Discordances between Auger and TA measures

As previously written, there is non-coincidence between Auger and TA measures around the energy of 10^{19} eV. As shown in figure 1.6, the spectrum of Auger is lower and shifted in energy respect to that of TA and this can be due to the different energy reconstruction technique of the two. The problem is that this difference takes the two experiments to observe a different composition of the spectrum (fig. 1.7 and 1.8) since TA observes substantially a proton composition while Auger measures a heavier composition. This fact does not allow the correct interpretation of the spectrum itself.

Figure 1.6. Focus on the energy spectrum around the ankle at 10^{19} eV with different experiments results.

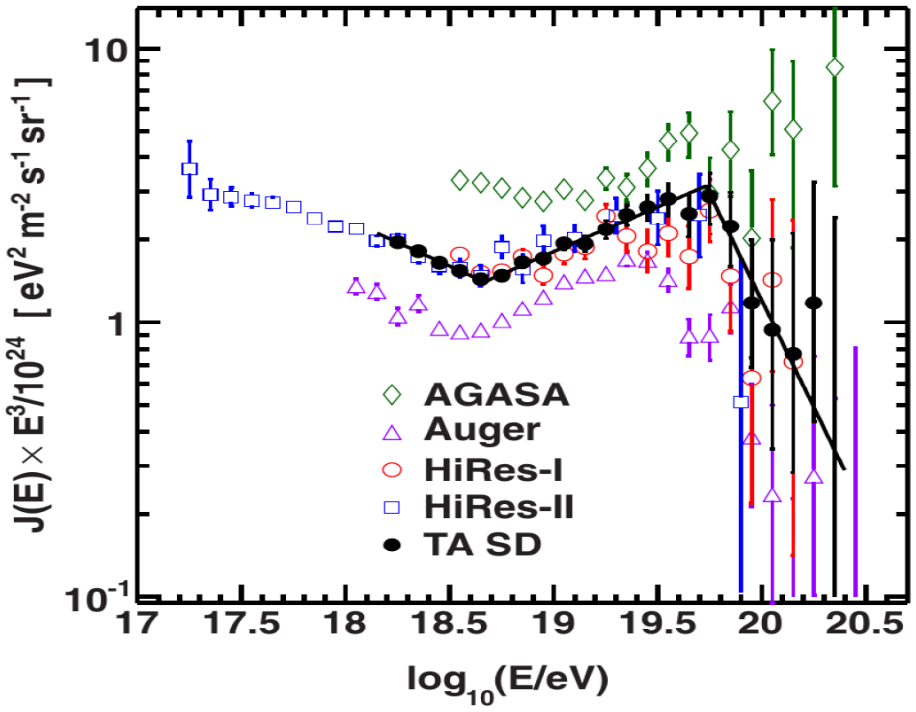

Figure 1.7. Composition at ankle energy for Auger [9]. Red lines represent proton composition for two different models, blue lines are the same for iron composition.

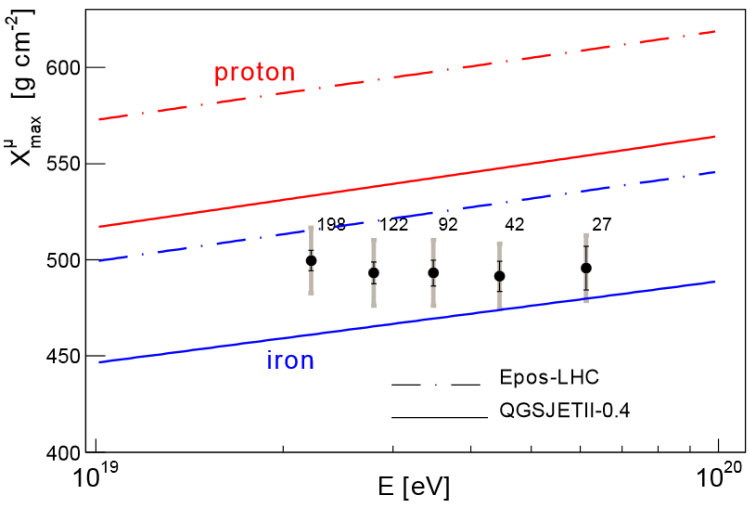

Figure 1.8. Composition at ankle energy for Telescope Array [10]. Black points are $< X_{max} >$. Blue line represents a proton composition, red one an iron composition. Grey points are X_{max} for each event.

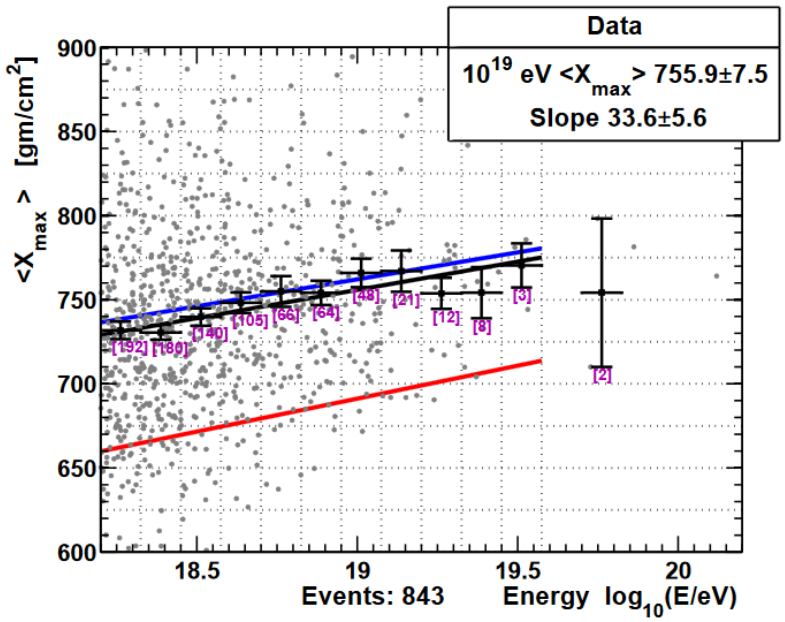

1.7 Neutrinos

Neutrinos are particles of three flavours having peculiar characteristics:

- neutral
- very low mass (not measured yet, probably under 1 eV)
- only weakly interacting
- oscillating in flavour
- very low cross section

Each neutrino is associated to a lepton ((e, ν_e), (μ, ν_μ), (τ, ν_τ)) with which it conserves the leptonic number. Neutrinos cross section allows them to travel a very large distance before interacting and their masses allow them to travel at nearly the speed of light. For these properties, they could be among the best "messengers" that we have in order to know about early universe. Neutrinos can be secondary products of other cosmic rays and a flux of this atmospheric neutrinos has been measured. Despite their abundance in the Universe, the predicted cosmological neutrino density is only slightly smaller than that of cosmic microwave background (CMB), their elusiveness makes necessary great mass detectors in order to have some interactions.

Figure 1.9. Neutrino flux at Earth [1]. Cosmological neutrino flux in **a** is strongly dependent on the model used. The Supernovae neutrinos in **c** and in **c'** are only for $\bar{\nu}_e$, since all other species have very similar fluxes. The **g** range is a prediction for astrphysical neutrino flux.

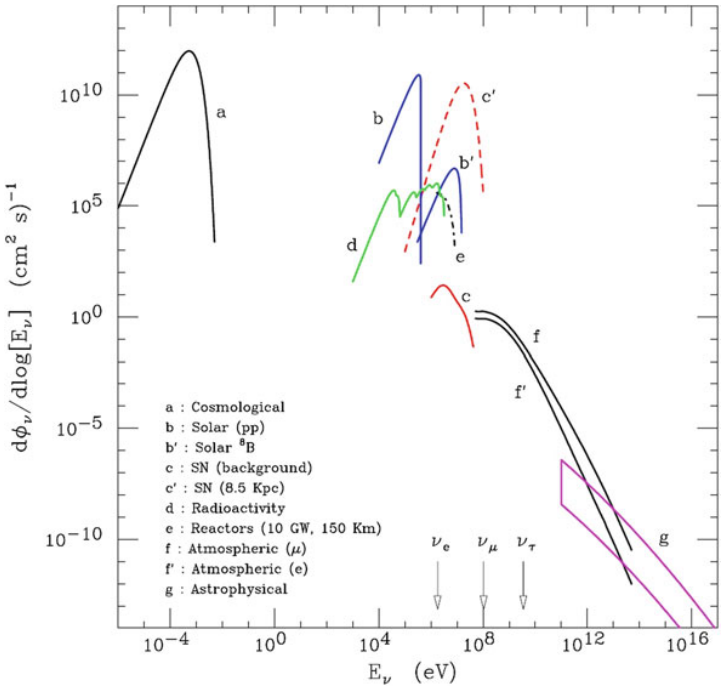

Neutrinos come mainly from hadronic processes in which weak interactions are present, in fact events like electro-magnetic cascades involve only electro-magnetic force. From proton interactions we have the so-called "photo-pion" production:

$$p + \gamma \to \Delta^+ \to \begin{cases} p + \pi^0 \\ p + \pi^+ \end{cases} \to \begin{cases} \pi^0 \to \gamma + \gamma \\ n \to p + e^- + \bar{\nu}_e \\ \pi^+ \to \mu^+ + \nu_\mu \\ \mu^+ \to e^+ + \nu_e + \bar{\nu}_\mu \end{cases} \tag{1.21}$$

At higher energy K mesons are produced too and their decay is as for π mesons:

$$\pi^{+(-)} \to \mu^{+(-)} + \nu(\bar{\nu}) \tag{1.22}$$

$$K^{+(-)} \to \mu^{+(-)} + \nu(\bar{\nu}) \tag{1.23}$$

Recently IceCube Collaboration showed [11] an evidence that, in addition to atomic nuclei and electrons cosmic rays, there is a flux of astrophysical neutrinos, whose origin is still not clear. In particular they showed (fig. 1.10) that the observed neutrinos flux is not describable by only atmospheric neutrinos and muons background. IceCube collaboration also tried to localize the sources of these neutrinos building a probability map (fig. 1.11), but they did not find any certain neutrino source. Nevertheless there are many proposed sources for neutrinos, both galactic and extragalactic. Galactic ones include microquasars, supernovae remnants and the galactic centre. Extragalactic sources could be active galactic nuclei and gamma ray bursts.

Figure 1.10. Neutrino energy spectrum from IceCube [11]. The data (black dots) and the best fit (grey line) have a different going respect to atmospheric neutrino fluxes.

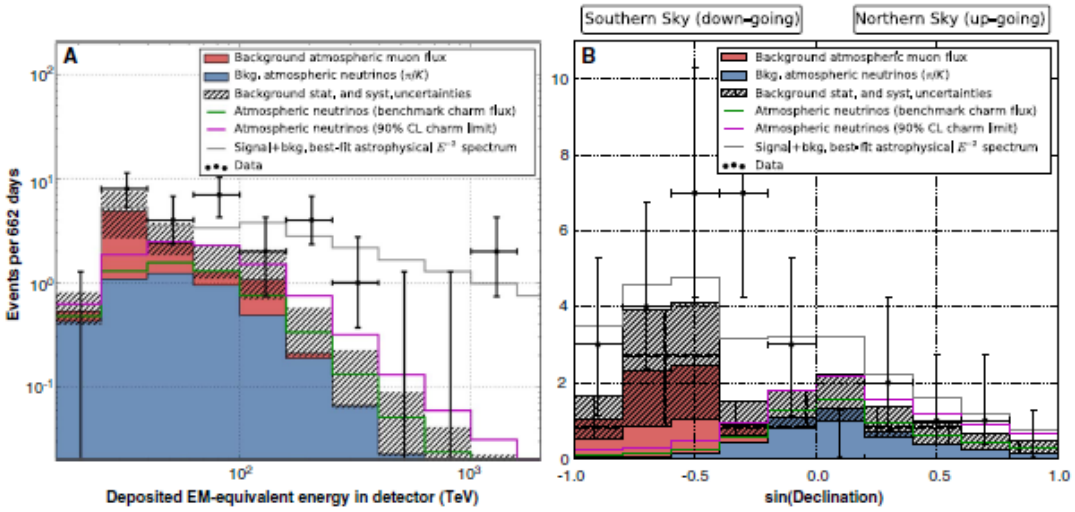

Figure 1.11. Probability map of sources by IceCube [11] where L in the color code indicates the likelihood.

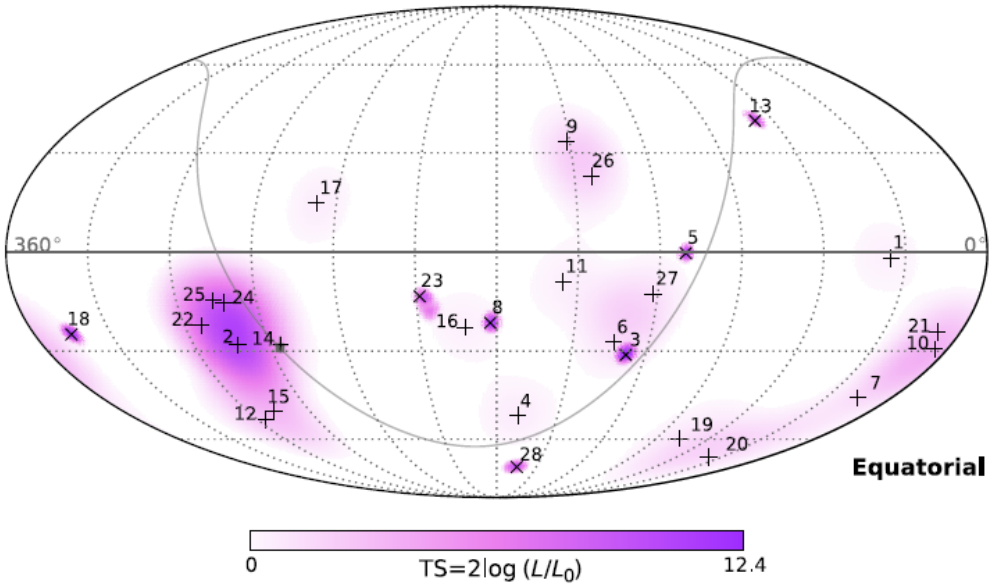

1.8 Detection of neutrinos

The very low cross section of neutrinos indicate that we need a very large detection volume to detect some of them. The best solution found at this problem it has been to use very large natural volumes of sea water (ANTARES, NEMO) or of the Antarctic ice (IceCube) as neutrino telescopes. Rough computations demonstrates that it is needed a $1\,\mathrm{km}^3$ volume to have a high enough number of detections. In water neutrinos interact in two ways, the so-called neutral current (NC) and charged current (CC). In the first one, after interacting with a nucleus, neutrino "survives" in the final state and a hadronic shower is produced. In the second case in the final state there is a lepton together with the hadronic shower.

$$\nu_l + N \rightarrow \nu_l + X \text{ (NC)} \tag{1.24}$$

$$\nu_l + N \rightarrow l + X \text{ (CC)} \tag{1.25}$$

where X indicates the hadronic shower. These interactions have a calculated cross section illustrated in fig. 1.13.

In the case of an electron neutrino, the electron produced in CC interactions causes an electro-magnetic shower. For muon neutrino CC interactions the muon produced travels a long path: for a ν_μ interacting with an energy of $E_\nu \sim 1\,\mathrm{TeV}$ the muon has on average an energy of $E_\mu \sim 500\,\mathrm{GeV}$, hence it can travel as long as $\sim 1\,\mathrm{km}$ and its deviation from the neutrino direction is

$$\Theta_{\nu-\mu} \leq \frac{1,5^o}{\sqrt{E_\nu[\mathrm{TeV}]}} \tag{1.26}$$

For this reason muon tracks are the best detectable events for point-like sources search, in fact electro-magnetic shower events have a much worse angular resolution

Figure 1.12. Representation of neutrino interactions in water: *a.* NC interaction. *b.* ν_e CC interaction with a hadronic shower and an electro-magnetic shower. *c.* ν_μ CC interaction, with the muon's long track. *d.* ν_τ CC interaction: the tauon decades after a short path, there are two hadronic showers.

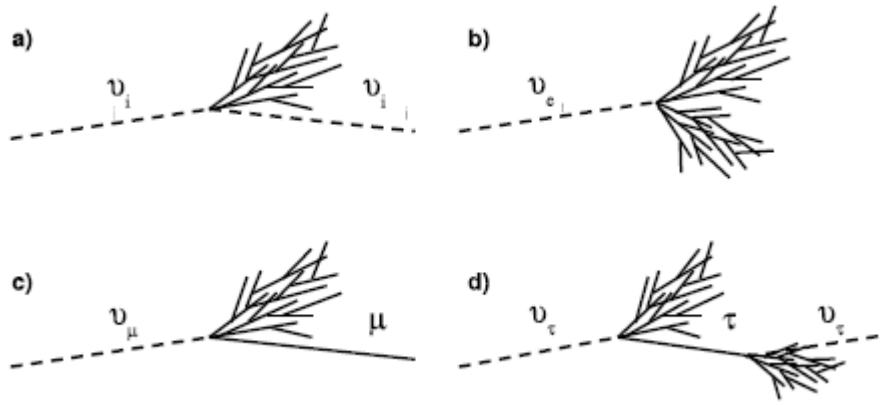

($\sim (10^o \div 15^o)$) due to the multiple interactions that characterize them. For the tau neutrino CC interactions, the tau produced decades after a short path causing another hadronic shower. This double hadronic shower is also known as "double bang".

An array of detectors distributed in the volume, detect the light produced by interactions. Showers are seen for electron neutrinos CC interactions, NC interactions and tau neutrinos CC interactions, Cherenkov light (explained in following chapter) due to the passage of muons at more than the speed of light in the medium can be detected for muon neutrino CC interactions.

The main problem of detecting neutrinos is the background, due to muons and neutrinos produced in interactions of other cosmic rays in the atmosphere. Obviously most of the atmospheric muons come from above because at high energy they cannot pass through the Earth and this makes difficult to detect astrophysical events coming from above (down-going) and make the neutrino telescopes better suited for the observation of the opposite hemisphere (hence the up-going events). Using the water as natural shield and a veto system, mis-recognized background detections are very limited.

1.8.1 Reconstructing a muon track

In this subsection we show an example of reconstruction of a muon track. A neutrino interacts at point (X_0, Y_0, Z_0, T_0) producing a muon. The track of the muon is described by

$$\begin{cases} x_\mu = X_0 + c_x \cdot s \\ y_\mu = Y_0 + c_y \cdot s \\ z_\mu = Z_0 + z_x \cdot s \end{cases} \tag{1.27}$$

where s is the arc length and

Figure 1.13. $\sigma N\nu$ value in function of ν energy from [12].

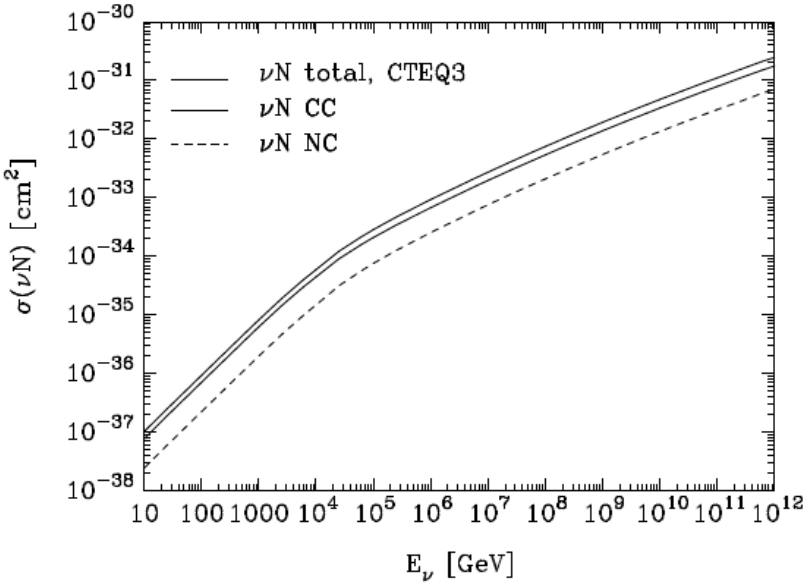

$$\begin{cases} c_x = \sin\theta\cos\phi \\ c_y = \sin\theta\sin\phi \\ c_z = \cos\theta \end{cases} \tag{1.28}$$

Cherenkov light induced by muon passage is collected by photomultiplier tubes (PMTs). The i-th photon hit the i-th PMT and it can be found the s value corresponding at the minimum distance

$$s_{min} = (X_{PMT} - X_0)c_x + (Y_{PMT} - Y_0)c_y + (Z_{PMT} - Z_0)c_z \tag{1.29}$$

from which the track point corresponding to the minimum distance is $x_\mu^i = X_0^i + c_i \cdot s_{min}$ and the minimum distance is

$$\Delta_{\mu PMT} = \sqrt{\sum_i (X_{PMT}^i - x_\mu^i)^2} \tag{1.30}$$

The photon having hit the PMT has travelled a path $d_\gamma^i = \Delta_{\mu PMT}/\sin\theta_C$ and the muon path until the emission of the photon is

$$d_\mu^i = d_{0\mu}\Delta_{\mu PMT}/\tan\theta_C \tag{1.31}$$

where $d_{0\mu} = \sqrt{\sum (X_0^i - x_\mu^i)^2}$. The time of arrival of the photon to the PMT is

$$t_i = T_0 + d_\mu^i/c + d_\gamma^i/(c/n) \tag{1.32}$$

Being j another photon emitted (and so another PMt hit) an experimental value $(\Delta t_{ij})^{exp}$ can be calculated as

$$(\Delta t_{ij})^{exp} = t_i - t_j = (d^i_\mu - d^j_\mu)/c + (d^i_\gamma - d^j_\gamma)/(c/n) \tag{1.33}$$

Given the time t_1 of the first signal from an event, a $(\Delta t_{1i})^{exp}$ can be calculated as an analogous theoretical value $(\Delta t_{1i})^{th}$. The set of coordinates ($\tilde{X}_0$, $\tilde{Y}_0$, $\tilde{Z}_0$, $\tilde{\theta}_0$, $\tilde{\phi}_o$, $\tilde{T}_0$) chosen is that minimizing the value

$$\sum \left(\frac{(\Delta t_{1i})^{th} - (\Delta t_{1i})^{exp}}{\sigma_{1i}}\right)^2 \tag{1.34}$$

1.8.2 The quality parameter Λ

The ANTARES collaboration has adopted the philosophy of reconstructing as many events as possible so, among them, there are also bad reconstructed events. To exclude these events it is necessary to have some parameters indicating the goodness of the reconstruction. As reported in more detail in [13], an important parameter is the likelihood function that indicate the probability to obtain a certain observed event. It is then calculated the value L of the likelihood at its fitted maximum. In fig. 1.14 is showed a plot of the values of $\log(L)$ in function of the number of degrees of freedom N_{DOF}. Another parameter is the number N_{comp} of the tracks compatible with the preferred track. For most of the badly reconstructed events it is $N_{comp} = 1$, while it can reach the value of 9 for well reconstructed tracks. The variable Λ combines all these parameters as follows:

$$\Lambda = \frac{\log(L)}{N_{\mathrm{DOF}}} + 0.1(N_{comp} - 1) \tag{1.35}$$

As can be seen in fig. 1.15, for values $\Lambda \gtrsim -5.5$, the majority of atmospheric muon events is excluded.

Figure 1.14. Scatter plot of the value of the likelihood function at the fitted maximum versus the number of degrees of freedom.

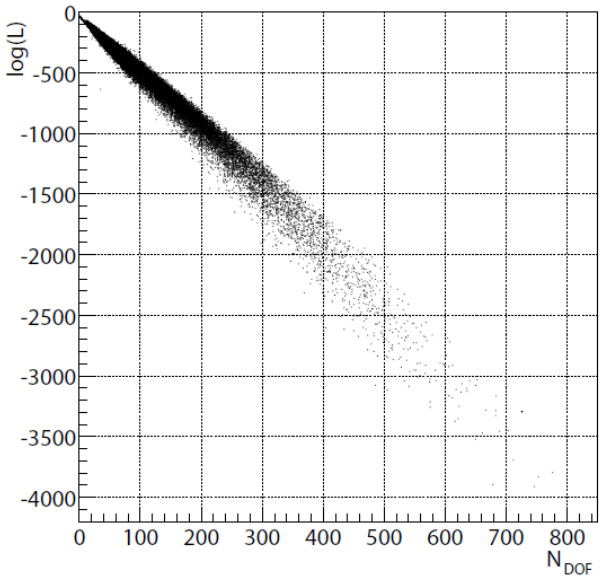

Figure 1.15. Distribution of the fit-quality parameter Λ [14]. Black dots are data. Blue circles are simulated atmospheric neutrino events. Pink circles are simulated atmospheric muon events.

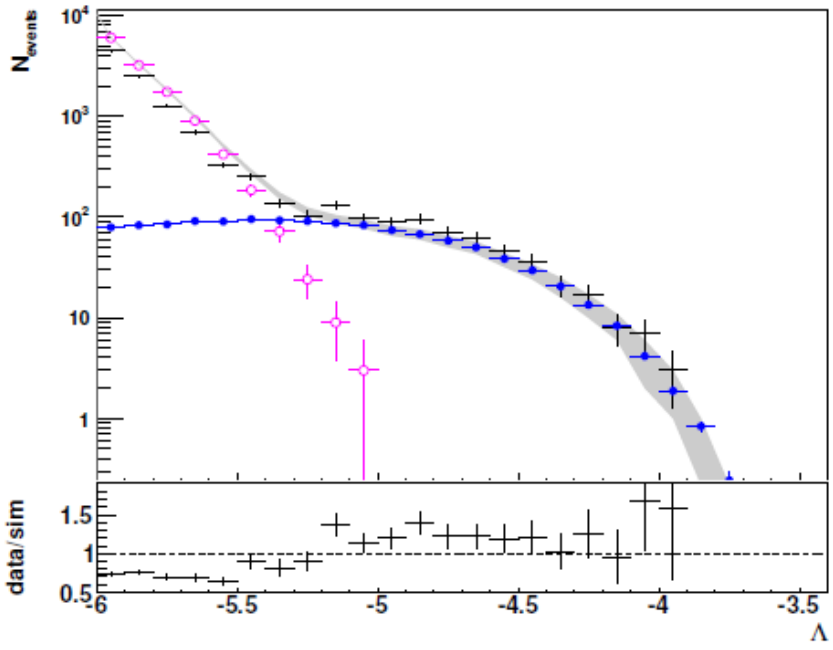

Chapter 2

Experiments

In this chapter the experiments involved in the thesis for cosmic ray data (Pierre Auger Observatory and Telescope Array) and neutrino data (ANTARES) are presented.

2.1 Pierre Auger Observatory

The Pierre Auger Observatory (PAO) [15] [16] is a detector of high energy cosmic rays situated at 1400 m a.s.l. near the town of Malargüe in Argentina. The structure is distributed over about 3000 km^2 in the area of Pampa. The location allows a good observation of the Southern Sky.

Auger is a hybrid detector since it works using mainly two different ways of detect cosmic rays: the Surface Detector (SD) and the Fluorescence Detector (FD).

2.1.1 Surface Detector

SD consist on 1660 ultra-pure water tanks of 12000 l each, distributed on all the 3000 km^2 area on a regular hexagonal grid at the distance of 1500 m each other. They are completely dark inside except for the Cherenkov light produced by the passage of particles, with the inner surface of the tanks being reflective. Each tank works autonomously. Cherenkov light is detected by three photomultiplier tubes with diameter of 9 in[1] mounted on the tanks. Signals are digitized at a 40 MHz sampling rate. Collected data are send to the basis by antennas. Trigger for an ultra high energy event starts when a minimum number of tanks detect particles. At trigger level the detection efficiency is 100% up from $3 \cdot 10^{18}$ eV. The aperture achieved for events having a zenith angle $\leq 60^o$ is 7350 $km^2\,sr^{-1}$ and increases of 30% including events with zenith angle up to 80^o. Duty cycle of SD is very nearly 100%, considering possible technical problems. When an extensive shower passes in the area, many tanks detect particles and so the energy of the shower can be reconstructed and the different time of arrival of the particles at different tank positions can help determine the trajectory of the shower. An important magnitude is that of $S(1000)$, that is the signal detected at 1 km from the intersection between the ground and the shower axis. The total signal is estimated with a fit. The

[1] 1 in = 25.4 mm, hence 9 in = 0.2286 m

energy is calculated from the particle density at given distances from the core and this proceedings is based on Monte-Carlo (MC) simulations, strongly dependent on the model used. This can cause problems like those discussed in subsection 1.6.2. Regarding the angular resolution, it increases with energy and zenith angle, being more detectors triggered.

2.1.2 Fluorescence Detector

FD is composed of 27 telescopes situated in 4 different places that can detect fluorescence light caused by the passage of the shower. The surface of the spherical mirrors of telescopes is $\sim 13\,\mathrm{m}^2$, with a field of view of about $30^o \times 30^o$. The mirrors focus detected light to a 440 pixels grid, each composed by an 8-stage PMT tube, with a 40 mm side-to-side hexagonal photocatode, and light collectors. The trigger system is composed by a hierarchy of more trigger levels. The FD can detect the light up to 15 km away. FD is very important to determine the direction and geometry of incoming showers and to recognize the primary particle nature, observing the distribution of light collected along the axis of the shower. Furthermore FD can measure the energy of showers being only slightly dependent on the models. Fluorescence detection has many advantages respect to surface detection, but its very reduced duty cycle limits its use.

2.1.3 Other detection systems

From November 2015 the AugerPrime Upgrade is active and consists in the installation of plastic scintillators on top of the Cherenkov tanks. These Surface Scintillator Detectors (SSD) cover all the area and they will improve the capability of studying the primary cosmic rays.

The Auger Engineering Radio Array (AERA) is a system of 124 radio antennas covering an area of $6\,\mathrm{km}^2$ spaced 250 m or 375 m apart from each other. AERA detect radio signals produced by highest energy showers and works in coincidence with SD an FD.

AMIGA is a system of 61 muon counters placed on a little area in a denser configuration, each one consisting on 64 plastic scintillators. It extends the energy range of Auger down to 10^{17} eV.

HEAT consists of telescopes similar to fluorescence telescopes but observing at greater heights.

2.2 Telescope Array

The Telescope Array (TA) [18] [19], situated in Millard County, Utah, USA on a $680\,\mathrm{km}^2$ area, uses a combination of ground array and air fluorescence techniques. It is a collaboration between former members of experiments HiRes and AGASA. Its position is favourite for observing the Northern Sky.

The TA observes events with energy greater than 10^{18} eV and it is a hybrid experiment consisting of 507 scintillators of $3.2\,\mathrm{m}^2$ located on a square grid of $1.2\,\mathrm{km}^2$ and three telescope stations with 12 to 14 telescopes each one on a 30 km triangle.

Figure 2.1. Auger map [17]. Single parts of the experiment are signed in red. Fluorescnce Detector stations are in blue, being the "rays" indicating the direction of view of the telescopes.

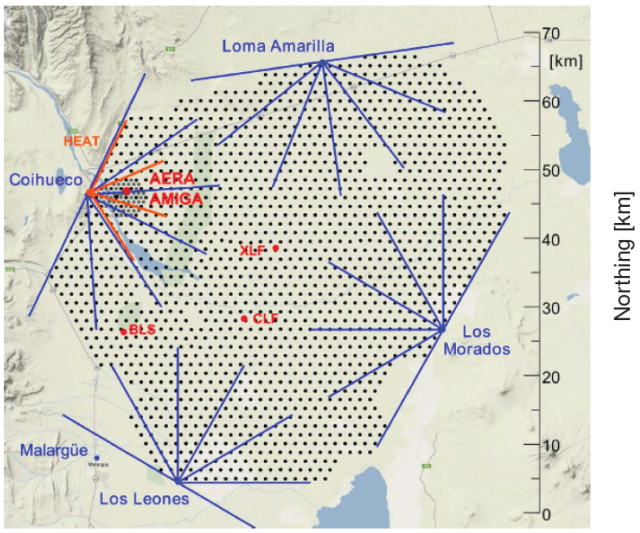

2.2.1 Surface detectors

The scintillator detectors are composed of two layers of $2\,\mathrm{m} \times 1.5\,\mathrm{m} \times 1.2\,\mathrm{cm}$ designed to interact with charged particles. When they pass, ultraviolet fluorescence light is released, gathered by optical fibers and directed onto photomultiplier tubes, one for each layer. Layers are separated in two along the 2 m dimension and every of the two parts is divided in four 25 cm long sub-units. The optical fibers are 47 cm long and 1 mm in diameter. The layers are wrapped in sheets and separated by a 1 mm thick steel plate. Scintillator detectors are self-powered through solar panels. There is a first level trigger locally on each counter. The second level trigger system consists in the detection of a minimum hits number by nearby detectors. For example for a more than three hits detection in three nearby detectors the trigger recognition time is 10 ms and the calculated trigger efficiency is 35% for protons with $E = 10^{18}\,\mathrm{eV}$ and 100% for protons with $E = 10^{19}\,\mathrm{eV}$. The energy resolution, estimated from analysing MonteCarlo simulations, is 27% at $10^{19}\,\mathrm{eV}$ and 19% at $10^{20}\,\mathrm{eV}$. Synchronicity of detectors is granted by a GPS communication system, data are transmitted to the tower bases by radio antennas. Calibration is done detecting the atmospheric muons, hitting the detectors 20 times per second and depositing a predictable amount of energy (that is the minimum ionization energy for muons).

2.2.2 Fluorescence detectors

There are three fluorescence detectors, one of which having been refurbished from HiRes, so it is for some aspects different from the other two. All telescopes have a combined spherical mirror of diameter 3.3 m and a focal length of 3.0 m. Detectors gather the light with mirrors and focus it onto a 256 PMT pixels camera. The field of view is a $15^o \times 18^o$ area so a pixel corresponds to $\sim 1^o$. Each station covers $\sim 30^o$

Figure 2.2. Map of Telescope Array. Red squares are Fluorescence detector stations.

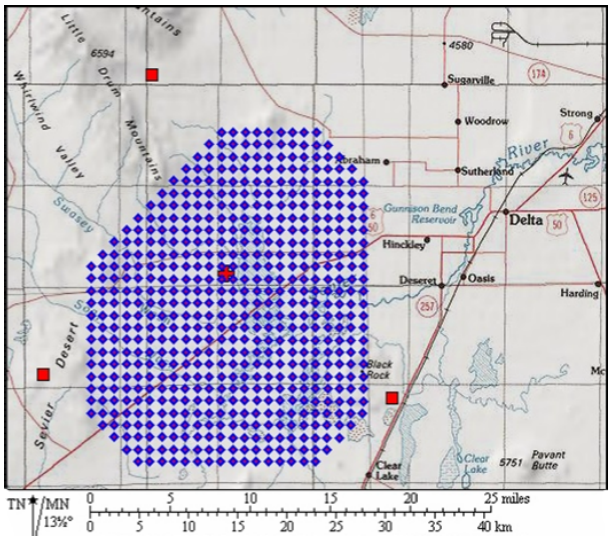

in altitude and $\sim 100^o$ in azimuth. Trigger is done with two or more Fluorescence Detectors or in hybrid mode with at least one FD and one SD. Calibration of telescopes is done observing Rayleigh scattered photons out of a calibrated N_2 laser. These telescopes can detect light emitted more than 30 km away.

2.3 ANTARES

The Astronomy with a Neutrino Telescope and Abyss environmental RESearch (ANTARES) [20] [21] is the largest underwater neutrino detector of the Northern Hemisphere. It is settled on the seabed at a depth of 2500 m at 40 km off Toulon in France. ANTARES is composed of twelve lines of active height of 350 m, and stretched by buoys, distant about 60 m each other for a total number of 885 PMTs covering an area of 0.1 km^2. The optimal distance between the PMTs was found through simulations in order to have the best possible neutrino detection efficiency. Each PMT consists of 3 Optical Modules (OMs) for detection of light, each of them pointing downwards at 45^o with respect to the vertical, aiming to optimize detection of up-going particles. The detector is linked to the shore station in La Seyne-sur-mer in France through 40 km of electro-optical cable. Each line is divided in 25 storeys each containing the three OMs except one that has hydrophones for acoustic detection instead of the top five storeys. There are many additional kinds of sensors for time and position calibration.

ANTARES has a very good angular resolution ($\sim 0.3^o$ for muon events above 10 TeV). This accuracy depends on different terms: the precision in knowing the position of the optical modules, the accuracy of the arrival time of photons on the optical modules, the precision in synchronizing all the optical modules signals. To make calibration possible, it is needed to know the positions of single OMs with a precision of 10 cm, considering that light travels 22 cm per ns in water. Time resolution is limited by the transit time spread of the signal in the PMTs and by dispersion of light in water. Several complementary calibration systems are

Figure 2.3. Illustration of ANTARES.

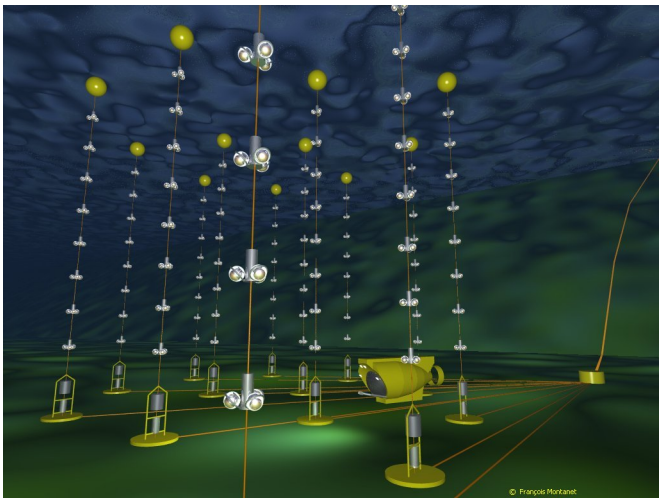

implemented.

For its position, ANTARES is favourite for observing the Southern Sky and for the inner part of the galactic centre. ANTARES has taken data in his final configuration since 2008 and it will continue until 2017, when the phase 1 of KM3NeT will be operative. ANTARES, because of its very good angular resolution, is optimal in looking for neutrino point-like sources but the ANTARES collaboration also works on measuring the diffuse flux. Being on the seabed, this experiment also involves different scientific branches in studying deep sea environment and biology, also to better understand the background signal detected, due not only to atmospheric secondary particles, but also to luminescence of some underwater species and to potassium decay.

The collaboration with many other experiments, either with other neutrino telescopes or in multimessenger projects, make its data more useful and its results more complete, as it will be shown in the next chapter.

2.4 Other experiments

2.4.1 Cosmic ray experiments

Many experiment have detected high energy cosmic rays during the years, each one contributing in many ways to the study of showers and overall to measure parts of the cosmic ray energy spectrum.

The Akeno Giant Air Shower Array (AGASA) was a Japanese detector built at the Akeno Observatory. It consisted of 111 surface detectors and 27 muon detectors and covered an area of 100 km^2. It worked till the first years of 21st century.

The High Resolution Fly's Eye Cosmic Ray Detector was operating in Utah from 1997 to 2006 using the Fluorescence detection technique. The main characteristic of this detector was the fly'eye structure of the collectors, able to measure the plan in which a shower lies. It worked together with the surface detector CASA and the muon detector MIA in the first hybrid experiment. Still today a HiRes mirror,

Figure 2.4. Schematic draw of IceCube. Grey regions are used for veto. *A.* IceTop. *B.* InIce.

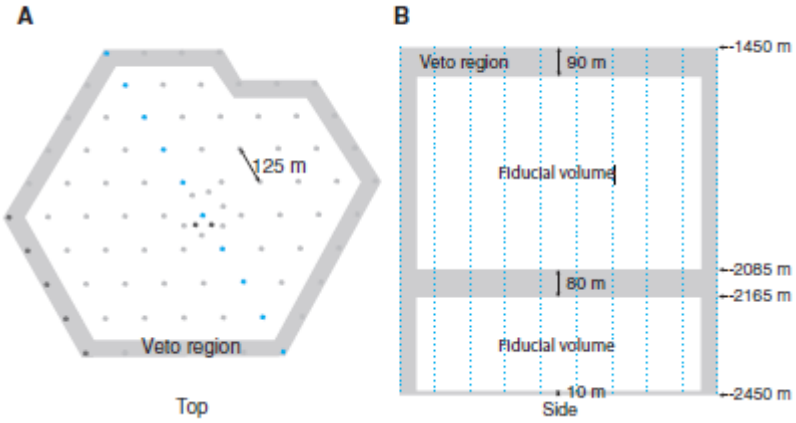

improved and upgraded, is used for the Telescope Array.

The Karlsruhe Shower Core and Array DEtector (KASCADE) was an experiment situated in Karlsruhe, Germany able to measure cosmic ray showers in the energy range $10^{16}\,\text{eV} \div 10^{18}\,\text{eV}$. It consisted of 252 detectors on a $200\,\text{m} \times 200\,\text{m}$ area. KASCADE-Grande was an extension of the detector to $700\,\text{m} \times 700\,\text{m}$ done with 37 EAS-TOP (an experiment at Gran Sasso, Italy) reassembled scintillators. It allowed to extend the energy range from $10^{14}\,\text{eV}$ to $10^{18}\,\text{eV}$. They were the first to see the knee at $10^{15}\,\text{eV}$.

2.4.2 IceCube and other neutrino experiments

The greatest active neutrino telescope and the first to reach $1\,\text{km}^3$ of volume is IceCube [22], settled at the Amudsen-Scott station at the South Pole, over the elder AMANDA. Its 86 detection lines have been immersed in the ice by hot water drills for a total of more than 5000 digital optical modules (DOMs). All the instrumentation was specially made to withstand freezing. The separation between the DOMs is 17 m and between the lines is 70 m. In addition to this InIce detector, IceCube is provided with a system of surface stations named IceTop that has mainly the function of veto on the down-going events. All the structure is displayed in fig. 2.4. IceCube can detect both muon tracks and cascade events and can work both with up-going and down-going events. To work with the last, it is necessary to put more tight conditions as for example a higher energy threshold, or considering only events with the neutrino interacting inside the detector. The detector is provided of some blue LEDs, useful for calibration and the study of optical properties of ice. The data acquisition is done at a sampling rate of 300 MHz and every module has two acquisition system working alternately to reduce downtime.The structure can also detect neutrinos of MeV energy, coming from supernovae in the Galaxy or in the Great Magellanic Cloud. As written yet, IceCube is the first experiment to have measured a neutrino astrophysical diffuse flux.

An important step towards underwater neutrino astronomy is the Baikal Neu-

trino Observatory, situated under the lake Baikal at about 1100 m of depth and 3.6 km off the shore. The advantage of this place is principally the fact that in winter the surface of the lake freezes and so it is possible to transport and install instrumentation under water from the surface. Baikal telescope is still active with 200 PMTs on 8 strings. The upgraded version should have 1000 PMTs in the future. This experiment began his study phase in early 1980s with the first PMTs settled under water to study the water properties.

NEMO was a "tower" of PMTs off the shore of Italian coast and began near ANTARES. This experiment, together with ANTARES and the NESTOR project, was the forerunner of the future KM3NeT consortium that expects to immerse its instrumentation for a km^3 neutrino telescope named ARCA (Astroparticle Research with Cosmics in the Abyss) off the shore of Capo Passero in Italy for the study of high energy neutrinos and a more compact telescope in France, off the shore of Lyon, for the study of low energy neutrinos named ORCA (Oscillations Research with Cosmics in the Abyss).

Chapter 3

Multimessenger astronomy

In the last years the collaboration between different astronomical experiments has become very important to improve sensitivity, capacity of analysis and understanding of cosmic processes by using different probes, such as photons, neutrinos, cosmic rays and gravitational waves. This is known as multimessenger astronomy and it can be a unique opportunity to discover astrophysical processes. Neutrino telescopes ANTARES and IceCube make great use of this way of working, with different combined analysis. In this chapter results from some of these analysis [20] are reported and details of few examples per kind are showed.

3.1 AGN: neutrinos and photons

Active Galactic Nuclei (AGN) are the main sources in the high energy photons universe. They are thought to be cosmic ray sources too. In particular blazars, those AGN that, besides the usual AGN photon emission, have jets in our direction of view, are among the best observable extragalactic sources.

Data of blazars from Fermi-LAT and TANAMI collaboration were analysed with IceCube events and several of these were found to be in the field of the two PeV events IC14 and IC20. They are two of the most energetic events detected by IceCube, with right ascension and declination respectively (265.6^o, -27.9^o) and (38.3^o,-67.2^o); both are shower events, hence they have a bad angular uncertainty (more than 10^o each). From the observed photon flux of six blazars in spatial coincidence with the two IceCube events an estimation of 1.9 ± 0.4 events at PeV energies in 662 days of IceCube observations was done. An extremely bright flare from a blazar was detected in the 50% error region of IC35 arrival direction. IC35 is the highest energetic event by IceCube, with energy of $\sim 2\,\mathrm{PeV}$.

A similar search has been performed using ANTARES data [23] in coincidence with six blazars. The whole blazar sample is classified as flat spectrum radio quasars (FSRQs). The fact that the two neutrino events considered are of PeV energy gives only a negligible probability for atmospheric origin for them. Both the events are assumed to be ν_e cascade and from photo-pion production model we expect a uniform in flavour neutrino flux. ANTARES uses only up-going muon events. From studies of the time-integrated and flavour-averaged exposure it results that ANTARES has a greater sensitivity in the zone of the blazars respect to IceCube.

It is predicted, and well accepted, that, for hadronic origin, neutrino flux from this sources is equal to photon flux regardless of the models (instead the shape of the flux is very model-dependent). Flux is considered to have a power-law spectrum with spectral index $-2.5 \leq s_\nu \leq -1.5$ for which ANTARES has a higher expected number of events respect to IceCube. In this range is also calculated a neutrino flux comparable with the total blazar photon flux. Strong limits on an E^{-2} spectrum was found. Two blazars have a neutrino coincident event but this observation is well within the background expected fluctuations. However the possibility that the two blazars are neutrino sources cannot be totally excluded.

A sample of about 50 blazars, mainly from Fermi-LAT and from other experiments (IACTs, H.E.S.S., MAGIC, and VERITAS), was analysed with ANTARES data. The lowest p-value was found corresponding to the blazar 3C 279 at coordinates $RA = 194.0^o$ and $dec = -5.79^o$. Anyway no significant post-trial p-values were found.

A similar method was used to search for neutrino emission during flares by galactic X-ray and γ-ray binaries. A sample of 34 selected sources were analysed with no significant detections. This allowed to reject with a 90% C.L. some models for hadronic processes

3.2 GRB and SGR: neutrinos, photons and gravitational waves

Gamma Ray Bursts (GRB) are fast intense flashes of light that are considered among the most powerful sources of the Universe. Their electro-magnetic spectrum ranges from the MeV γ-rays to infra-red, they are thought to be gravitational wave (GW) sources and to have relativistic outflows of hadronic origin, hence also emitters of cosmic rays and neutrinos. There are different models for GRBs [24]. They could be due to accretion onto a compact object or rapidly rotating neutron stars. GRBs are in general of extragalactic origin and the rate of such events in the observable universe is a few per-day. A multimessenger approach can help to better comprehend physical processes involved in GRBs and this can be done with both follow-ups and real time alerts.

The ANTARES collaboration looked for coincidences between 296 bursts and neutrino events during the period 2008-2011. No such coincidences were found and limits were set on bulk gamma factor and baryonic loading of the burst jets.

A follow-up [25] was done looking for cosmic neutrino events in a window of ± 500 s around the gravitational wave event GW150914 detected by the two advanced-LIGO interferometers in Hanford, WA and Livingston, LA. The event was produced by a binary black hole merger at a luminosity distance of 410^{+160}_{-180} Mpc with the two masses of 36^{+5}_{-4} $M_\odot$ and 29^{+4}_{-4} $M_\odot$ for a total event duration of 0.2 s. For this type of event electro-magnetic and neutrino emissions can exist only if the event occurs in baryon dense environment, hence there has to be a black hole accretion disk. The search was done despite this situation is unlikely for the observed event.

The same analysis was performed with the IceCube detector and 3 events from Northern and Southern Sky were found in the observed window. Such number of

events is consistent with the expected background of 4.4. ANTARES detected no events with an expected background of 0.014 events. However none of the IceCube events has a directional coincidence with the GW 90% confidence level sky area. as outcome a standard frequentist neutrino spectral fluence upper limit was set for this type of GW sources.

Since angular resolution of neutrino detections ($\sim 1\,\mathrm{deg}^2$ for IceCube and $\sim 0.2\,\mathrm{deg}^2$ for ANTARES) is much smaller of that for GW events ($\geq 100\,\mathrm{deg}^2$), joint neutrino and GW event can greatly improve the efficiency of electro-magnetic follow-up, reducing the sky area to be covered.

Soft gamma repeaters (SGRs) are sources of short bursts of gamma rays emitted at irregular intervals. They also occasionally emit giant γ/X -ray flares. They can be detected within a few megaparsec and so mainly from the Galaxy. They are thought to be highly magnetized neutron stars with a tectonic activity. A seismic event (starquake) in such an environment produces GW emission, and furthermore magnetic field reconfiguration causes γ and X-ray emission and probably accelerates atomic nuclei that produce high energy neutrinos.

3.3 Neutrinos and ultra high energy cosmic rays

It is important to find out if there is a correlation between ultra high energy cosmic rays and neutrinos because it is known neutrinos can be produced in hadronic processes. The increase in detecting capacity in both the fields encourage to carry on with these studies. A study of correlation between PAO and TA cosmic ray data and ANTARES neutrino data will be done in this thesis.

A similar study has been performed in [26] considering data of many different cosmic ray detectors, mainly PAO and TA, and IceCube data (35 neutrino events). More details on this data analysis will be given in chapter 5. They built a test statistic called $\delta\chi^2$ evaluating the angular distance between couples formed by a neutrino and a cosmic ray. Through a frequentist approach they calculated the p-value of correlation with different selections of cosmic ray events. They also tried to associate matching cosmic ray events to sources from the Swift-BAT X-ray catalog and Kühr radio catalog in the GZK volume (in addition to protons interacting with CMB photons, neutrino sources luminosity and weak nature of neutrinos does not allow identifications of too far neutrino sources), finding a significant correlation, mainly with Seyfert galaxies. No correlation was found with AGN in Fermi-LAT catalog. In the end, they estimated the needed cosmic ray and neutrino luminosity to produce observed events and compared them with X-ray luminosity of the corresponding sources in catalogs. They found that to accelerate protons to $E = 10^{20}\,\mathrm{eV}$ it needs a considerable fraction of Eddington luminosity ($L_{Edd} = 1,3 \cdot 10^{46}(M_{BH}/(10^8 M_\odot))\ \mathrm{erg} \cdot \mathrm{s}^{-1}$ where M_{BH} is the mass of the black hole) of the sources to be non-thermal (and then to be stored in magnetic field and accelerate particles). In some cases the required luminosity exceed the Eddington limit.

3.4 TAToO: real time alerts

The Telescope-ANTARES-target-to-opportunity is a near-real time collaboration between ANTARES and optical robot telescopes and the Swift-XRT (X-Ray Telescope). When a sufficiently high energy (for X-ray the threshold is higher) up-going event is detected a fast alert message is generated and sent to the telescopes within a few seconds. Since now no associated transient event were detected and limits on astrophysical origin of neutrinos were set.

It is important to note that the rapidity of alerts is very important for example in combined search with GRBs, because a delay of only one hour can prevent the detection of GRB light and foil the association of two events.

Astrophysical Multimessenger Observatory Network (AMON) is going to be realized and is planned for real-time correlation between photons, low and high energy neutrinos, cosmic rays and gravitational waves.

3.5 Searches with Fermi Bubbles

A multimessenger analysis can be done also with extended sources like Fermi Bubbles. They are giant regions characterised by a γ-ray emission extending out of the galactic centre with a hard E^{-2} spectrum. In some models they have been proposed to be hadronic acceleration sites. From these regions, named Fermi Bubbles, we expect neutrinos due to p-p collision. In these models cosmic rays collide with galactic Interstellar medium to produce pions, hence neutrinos, and a background of γ-ray photons.

A study with IceCube high energy starting events in $E > 100\,\mathrm{TeV}$ range with angular reconstruction consistent with this region was done. The measured neutrino flux is consistent with γ-ray flux from the region. Anyway large uncertainties and the low number of events don't allow certain results.

ANTARES looked for coincidences in a region of $|l| < 40^o$ and $|b| < 3^o$ comparing the number of events in the area of the two Fermi bubbles ("on-zone") with that of three similar regions with no expected signals ("off-zones") [14] (fig. 3.1). The off-zones give data in order to estimate background hence to compare fluxes with the on-zone flux. At first the flux of ν and $\bar{\nu}$ was estimated. Neutrino data were selected with cuts based on the so-called tracking quality parameter Λ and on the reconstructed energy of th muons E_{rec}. Furthermore data with at least 10 detected photons and with the angular error estimate[1] $\beta > 1^o$ are selected. After a blind criteria selection, events with $\Lambda > -5.14$ (substantially it removes atmospheric muon events) and $\log_{10}(E_{rec}[\mathrm{GeV}]) > 4.03$ are selected. An excess of events of $1.2\,\sigma$ is founded in the on-zone and a small excess of high energy events is seen respect to the average from the off-zones and from the atmospheric neutrino simulations.

[1]The angular error estimate is an evaluation of the error in reconstructing the direction of an event, that is in general $\beta < 1^o$ for well reconstructed muon tracks and of the order of $\sim 10^o$ for cascade events

Figure 3.1. Map of Fermi Bubbles (shaded area) and the three off-zones.

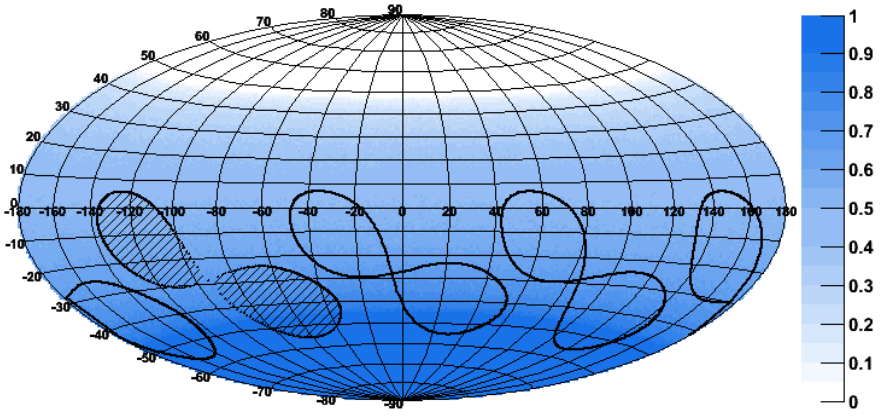

3.6 IceCube and ANTARES

The two neutrino telescopes are in constant collaboration to improve the capacity of discovery and give more usefulness to single experiment data. The complementarity of the two experiments is not only in the observed sky areas but also in the energy range; in fact ANTARES has a better sensitivity in the $(1 \div 100)$ TeV region, while IceCube is better from 100 TeV (fig. 3.2).

In particular ANTARES looked for events in the zone of the galactic centre where IceCube found a cluster of events that is not explainable with only background contribution. An analysis was done with the technique of on- and off-zones without finding any excess. ANTARES rejects at 90 % confidence a flux from this region expected to produce three or more of the IceCube events in the cluster. Limits on the neutrino flux from sources in this zone and on the spectral index of the flux were calculated.

Another study [27] was done using 5 years of data from ANTARES and 3 years of data from IceCube. The optimisation of the ANTARES sample was done through the quality parameter Λ, the angular error estimate β and the zenith angle θ. Since the search was done in the Southern Sky the selection on IceCube is on down-going events, so only well reconstructed muon tracks are taken and only with very high energy. A likelihood function to calculate a maximum likelihood ratio estimation was built, taking into account energy and direction of events by the two detectors and also the different response of the two detectors is taken into account (fig. 3.3). Two different analysis were done: the first was looking for excess at 40 pre-selected neutrino source candidate locations taken from the search for point-like sources of single experiments, the second was a full sky search on $1^o \times 1^o$ steps over the whole Southern Sky. In the first case no significant clusters of events are found. The best pre-trial p-value was found corresponding to a cluster found in a precedent ANTARES point-like sources analysis. The post-trial p-value is 0.7 σ, since 24% of pseudo-data sets constructed randomizing right ascension of data has a higher best pre-trial p-value than that of real data. Also in the second case no significant

excess was found. The best pre-trial p-value is in correspondence with the source HESS J1741-302 and the post-trial p-value is 1.2 σ (11%). It was seen that point-like source sensitivity has improved by a factor of two in a great region of the sky centered at the galactic centre, and the gain in a background dominated sample is $\sqrt{2}$.

Figure 3.2. Muon tracks effective area for ANTARES and three configurations of IceCube (dashed lines).

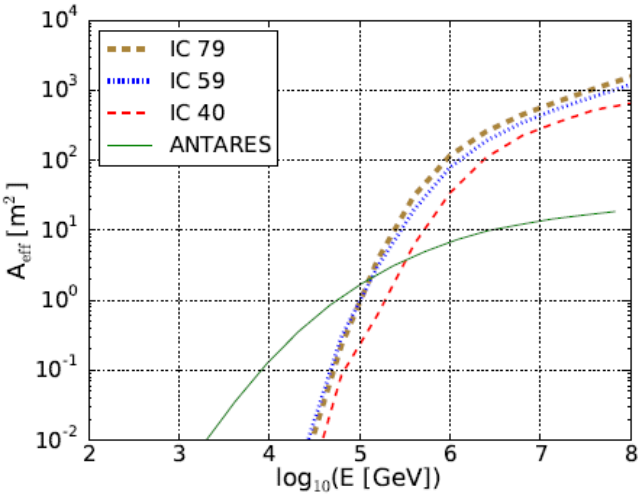

Figure 3.3. Fractional number of source events for ANTARES and IceCube with a spectral index $\gamma = 2,0$.

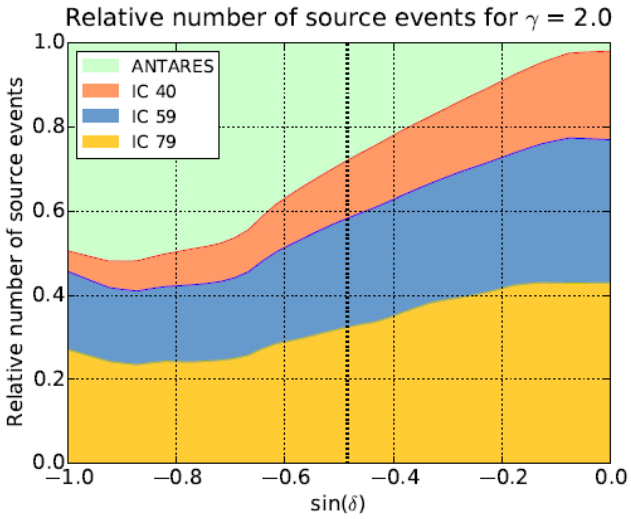

Chapter 4

Evaluation of cosmic rays propagation in magnetic field

The effect of magnetic field on cosmic rays discussed in chapter 1 leads to pursue a way to measure how much particles are influenced. We choose to rely on a largely used simulation tool called CrPropa as described below.

4.1 CrPropa

The investigation for the origin, nature and acceleration of ultra high energy cosmic rays requires to take into account many different aspects: it is needed to define models to describe cosmic ray flux and distribution, energy spectrum and mass of particles, magnetic fields, interactions with photon backgrounds (mainly Cosmic Infrared Background, CIB and Cosmic Microwave Background, CMB). CrPropa [28] is a complete tool of simulation for the propagation of ultra high energy cosmic rays. The reason of its development was the lack of such a tool that could take into account propagation effects, energy losses and magnetic field deflections at the same time and CrPropa offers a variety of different possibilities to study many variegated situations.

In this work we used CrPropa for two scopes: understand the influence of galactic magnetic field of UHECRs reconstructing back the trajectory of a particle inside the galaxy and calculate average deflection of particles in a simple model for extragalactic field.

4.1.1 Galactic backtracking

CrPropa can reconstruct back the trajectories of particles in a galactic environment. Substantially the anti-particle of that which have to be treated is tracked back from the arrival position along the arrival direction. The program can also calculate the uncertainty on the position found for the particles, basing on the original uncertainty and on the model. The galactic magnetic field model used for this simulation is that described in subsection 1.3.1. In addition to this coherent component, the striated and turbulent component are included. These two components are randomly calculated by the tool basing on limits given by models, as already written

Figure 4.1. Map of deflections due to galactic magnetic field in equatorial coordinates. Colored rounds are observed angular positions of cosmic rays with energy as in the colorbar. Red bordered rounds are angular positions of the cosmic rays at the galactic border. Green lines link each observed point with its correspondant point at galactic border. Dashed black line is the galactic plane.

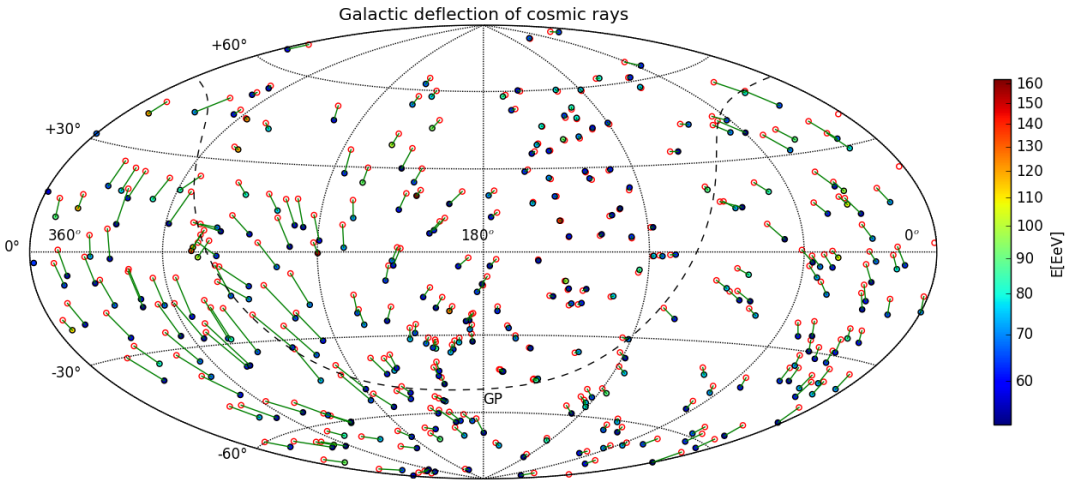

in subsection 1.3.1. We did the simulation setting protons as probes and the Sun as observer position.

Fig. 4.1 shows the results of the simulation. A zone with very small deflection can be noted north of the galactic plane in the right ascension range $120^o \div 180^o$. As expected, cosmic rays coming from the same area have similar deflections, supposedly to have passed through near the same magnetic field. Deflection is smaller for higher energy events. Distribution of deflection angles is in fig. 4.2. Mean deflection is $(4.66 \pm 3.28)^o$ and mean angular uncertainty is $(1.38 \pm 0.81)^o$. The list of events with new angular positions is in appendix.

4.1.2 Extragalactic propagation

We simulated the propagation of nuclei in different turbulent magnetic field environments with a Kolmogorov spectrum. The root mean square (rms) intensity of the field can be chosen and simulation with rms intensity equal to 1 and 4 nG were performed. For easiness we will denote the two just written magnetic field environments respectively as MF1 and MF4. The energy range covered goes from 5 EeV to 170 EeV in steps of 5 EeV on a distance of 25 Mpc. Simulations were done on five different types of nuclei: H, He, O, Si an Fe. Simulations include interactions with background photons such as photopion production, photodisintegration and electron pair production. Magnetic field is built on a grid of $256 \times 256 \times 256$ bins of 30 kpc spacing and the trajectory is simulated step by step (steps are of order of kpc and are not constant along the trajectory). For every energy step 10 000 nuclei are simulated and average deflection and root mean square are calculated. Results are shown in figs. 4.3 and 4.4.

All nuclei undergo the interactions with photon background. In the case of

Figure 4.2. Distribution of deflection angles due to galactic magnetic field.

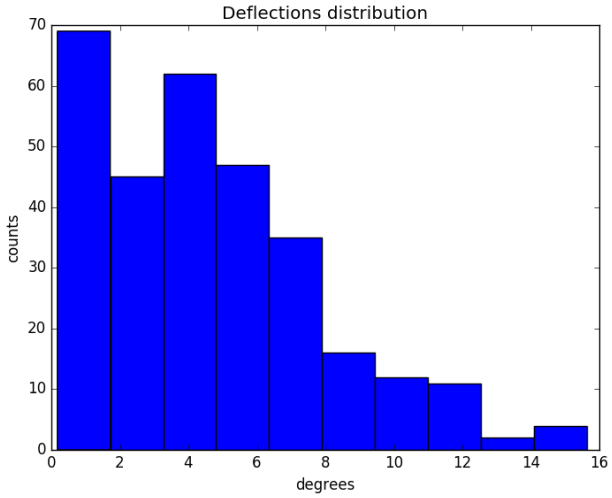

protons we consider also interactions when calculating the deflection angle, for this reason energy losses are not negligible, so average final energy of protons is reported, together with a linear function $x = y$ for comparison, in fig. 4.5 . The other nuclei instead in interactions change their nature, so they cannot travel for all the 25 Mpc, having a sort of "free path length" $l < 25\,\text{Mpc}$. In this case we report average free path length in fig. 4.6 and put upper limits on the deflection angle doing simulations with Iron on 25 Mpc excluding interactions (in figs. 4.3 and 4.4), hence allowing the Iron to travel the whole distance. Iron was chosen because it is the nucleus with the highest possible Z, so it is the most subjected to magnetic field deflection. For a right comparison, also proton points in figs. 4.3 and 4.4 are calculated excluding interactions.

The mean deflection angle seems to be dependent on the charge Z of nuclei and on the magnetic field intensity. As expected deflection decreases at raising energy. As can be seen, the energy losses for protons(fig. 4.5) and the probability of interaction (free path length in fig. 4.6) seem to be only dependent on the starting energy of travelling nuclei (hence not on the magnetic field). The energy losses are higher at higher energy. The trend of trajectory lengths at increasing energy seems to follow a well defined shape, similar for all nuclei. In fact we observed a coincidence between the energy threshold for electron pair production and the steepening in free path length. The Telescope Array collaboration calculated the energy threshold for electron pair production from interactions between protons and photons of the CMB and they found it to be $E^H_{p\gamma} = 4.6\,\text{EeV}$. For heavier nuclei we consider the energy as parted between all nucleons, so a general energy threshold for pair production can be written as $E^A_{p\gamma} = A \cdot E^H_{p\gamma}$. This is the same energy at which the steepening in free path length is seen on our plots, so it is possible that there is a correlation between the two things.

To study the correlation between UHE cosmic rays and neutrinos in presence of deflection due to magnetic field, we choose to use proton data including interactions from MF1 (fig. 4.7), taking into account considerations done in subsection 1.3.2.

Figure 4.3. Deflection of H and Fe nuclei considered in MF1.

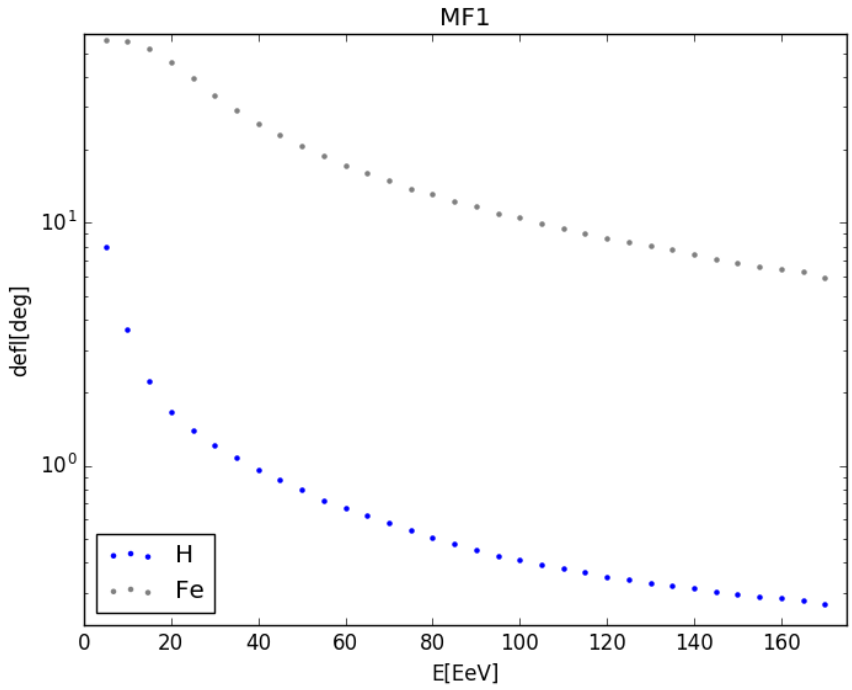

Figure 4.4. Deflection of H and Fe nuclei considered in MF4.

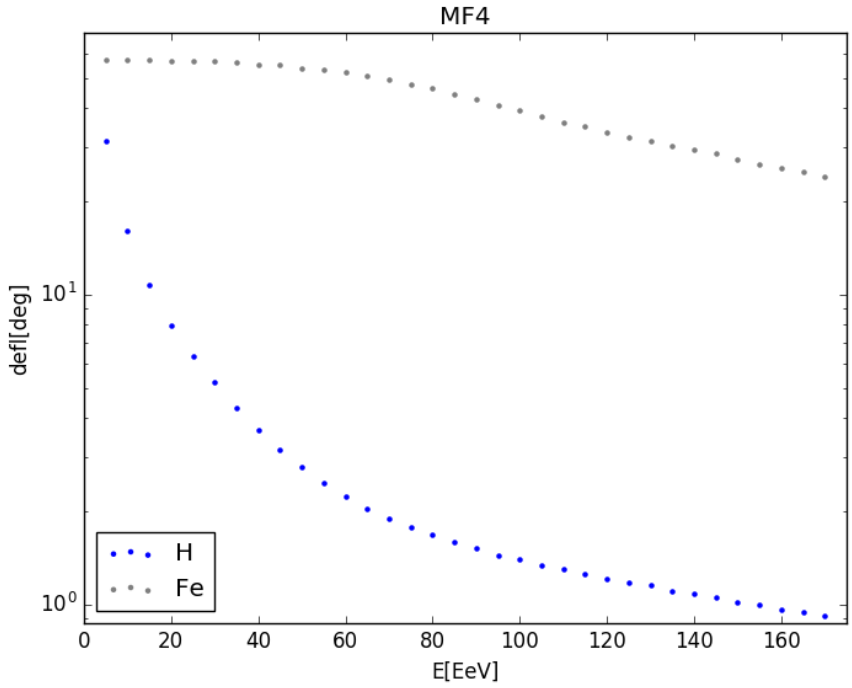

Figure 4.5. Final energy of protons. Magnetic field environment is indicated in figures.

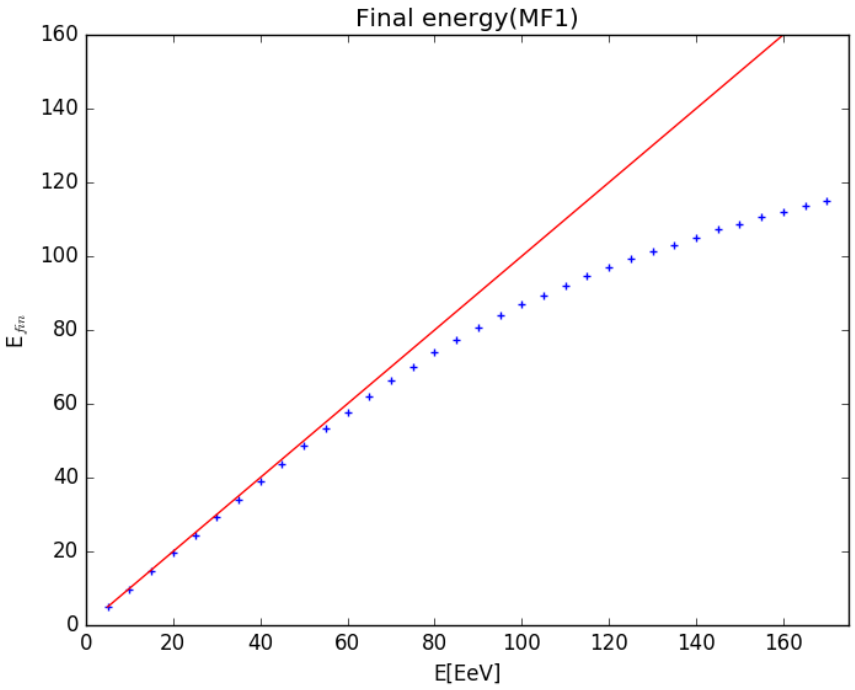

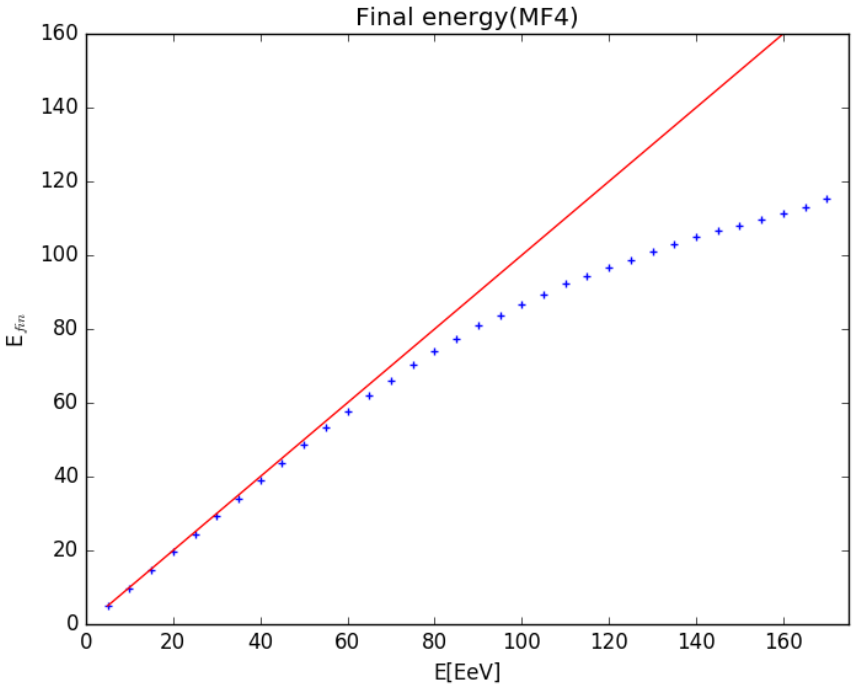

Figure 4.6. Length of trajectories travelled by heavier nuclei. Magnetic field environment is indicated in figures.

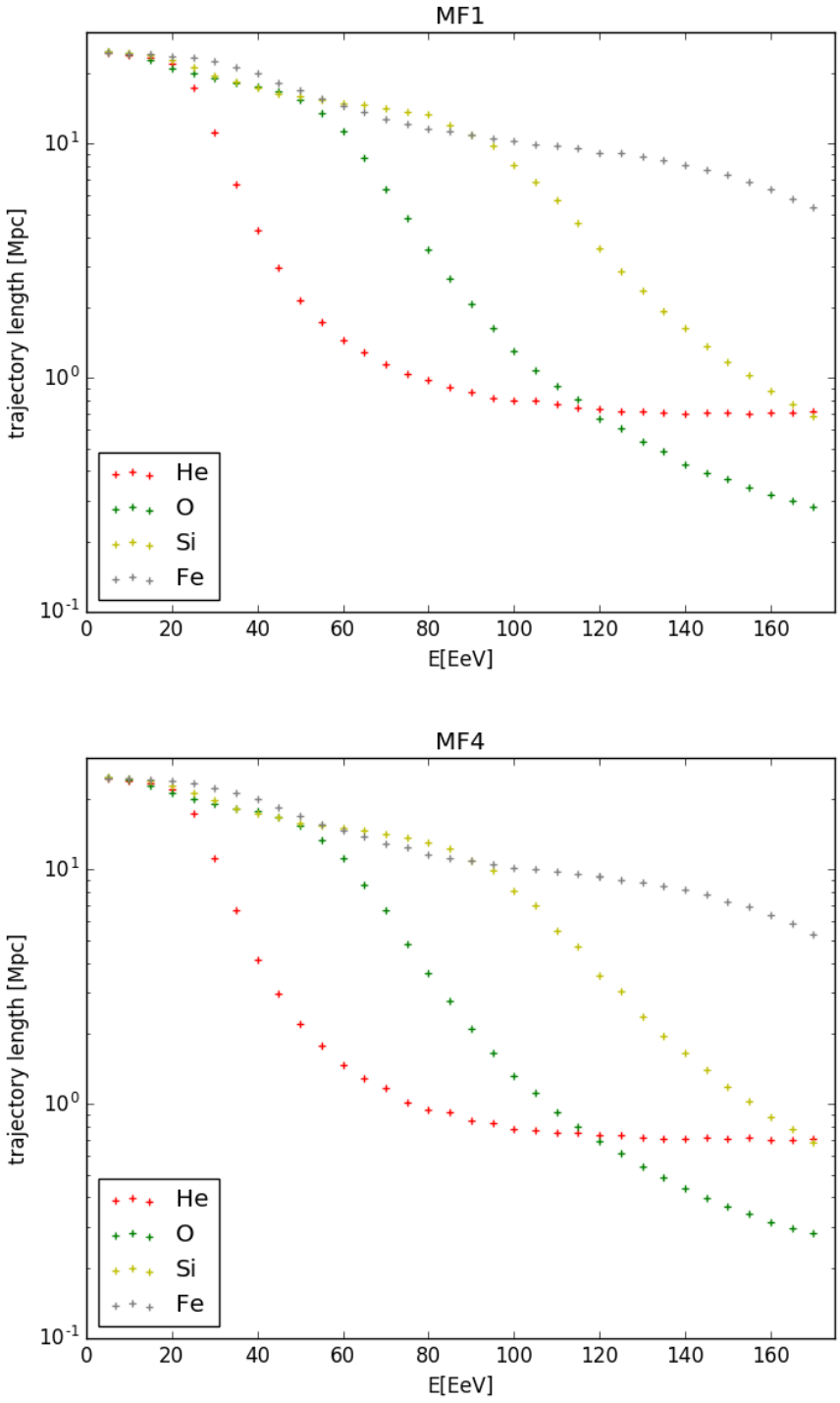

Figure 4.7. Plot of deflection angle for protons in MF1 including interactions.

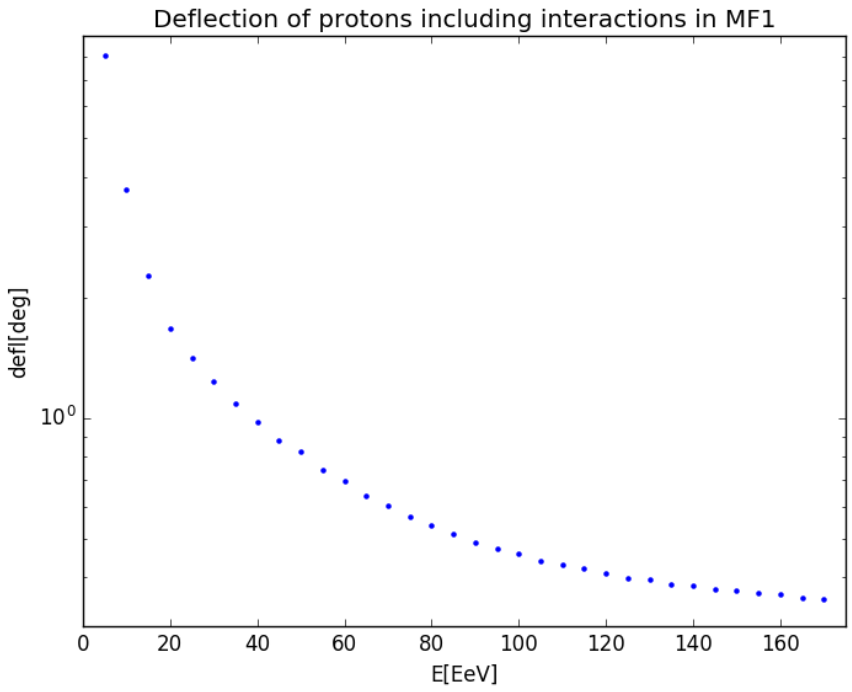

Chapter 5

Data analysis

The aim of this thesis is to study the correlation between cosmic ray events detected by PAO and TA and neutrino track candidates detected by ANTARES. In this chapter the data samples and the analysis strategy will be explained.

5.1 Data

5.1.1 Cosmic ray events

The Pierre Auger experiment published recently a compilation of the properties of their most energetic events [29]. The sample is composed of 231 events with $E > 52\,\text{EeV}$ detected from 2004 till 2014, mainly from the Southern Sky (due to PAO position). The angular uncertainty is 0.9^o for each event. A map of the events with their energy is reported in fig. 5.1.

Figure 5.1. Map of events from Pierre Auger Observatory.

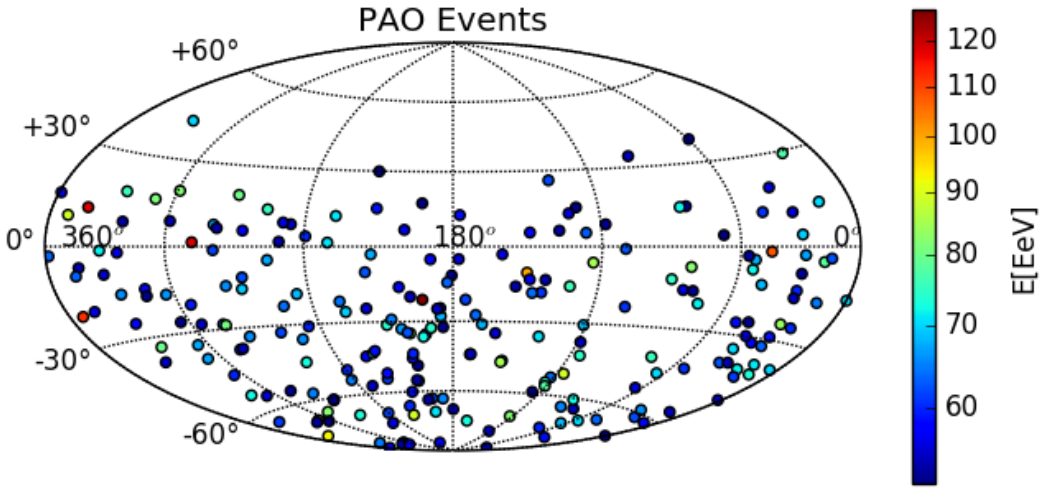

Also the Telescope Array experiment has provided similar information for 72 events with $E > 57\,\text{EeV}$ detected from 2008 to 2013 [30]. These events are displayed

in the map of fig. 5.2. In this case the angular uncertainty for each events is 1.5^o. Events are mainly from the Northern sky.

Figure 5.2. Map of events from Telescope Array.

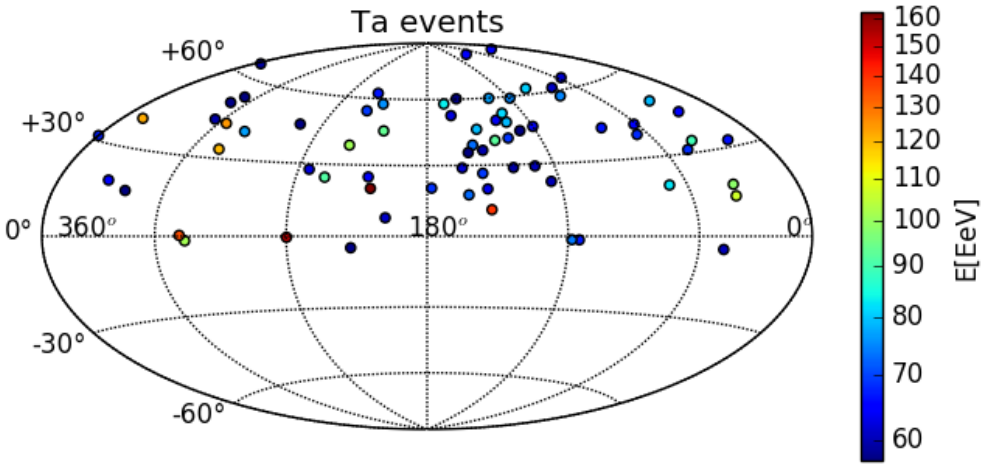

5.1.2 Neutrino events

As neutrino events we use those detected and reconstructed as μ tracks by ANTARES during his activity from 2007 to 2010. We consider 233 events with $E > 500\,\text{GeV}$. We selected events with angular uncertainty[1] $\beta < 1^o$ (on average $\sim 0.5^o$) and $\Lambda > -5.2$. The map of events is shown in fig. 5.3.

Figure 5.3. Map of selected ANTARES events.

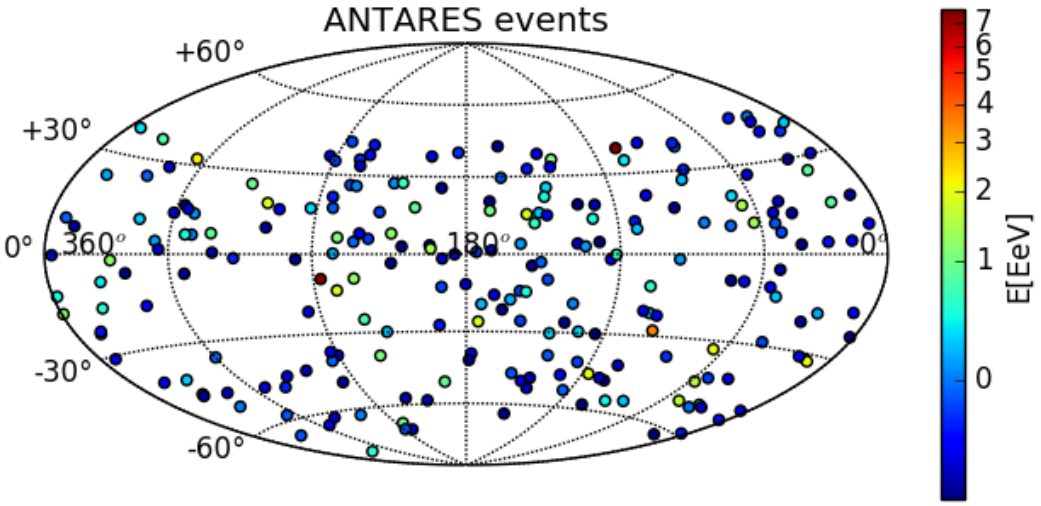

[1]Definition of the angular error estimate in section 3.5

5.2 Strategy of analysis

In this section we will describe the statistical method [26] to search for ν-CR correlation, following what we already introduced in section 3.3.
Right ascension (RA) and declination (Dec) of events are associated to unit vectors on a sphere as

$$\hat{x} = (\sin\theta\cos\phi, \sin\theta\sin\phi, \cos\theta)^T \tag{5.1}$$

where $\theta = RA$ and $\phi = \pi/2 - Dec$. An invariant measure of the correlation between a cosmic ray event j and a neutrino event i is the angle γ_{ij} between the two matching vectors:

$$\gamma_{ij} = \arccos(\hat{x}_{\mathrm{UHECR}j} \cdot \hat{x}_{\nu i}) \tag{5.2}$$

Since the PAO and TA experiments did not claim to have in their samples a couple of events coming from the same direction we do not expect to have a good angular matching between a neutrino and more than one cosmic ray. So for each neutrino $\hat{x}_i$ we will search for the better correlation between its direction and the one of all j cosmic rays using the value

$$\delta\chi_i^2 = \min_j(\gamma_{ij}^2/\delta\gamma^2) \tag{5.3}$$

where j indicate the UHECR and $\delta\gamma$ is defined as

$$\delta\gamma = \max(\delta\theta_{\mathrm{UHECR}}, \delta\theta_\nu) \tag{5.4}$$

where $\delta\theta_{\mathrm{UHECR}}$ and $\delta\theta_\nu$ are those indicated respectively in subsection 5.1.1 and subsection 5.1.2. Since the maximum uncertainties for neutrinos (a minority of the cases) are in the range $0.9^o \div 1^o$ while the minimum uncertainty for cosmic rays is that for Auger events that is 0.9^o, in the majority of the cases is $\delta\gamma = \delta\theta_{\mathrm{UHECR}}$. According to what has been done in [26] it is considered a "good match" a value of $\delta\chi_i^2 \leq 1$. We define N_{corr} as the number of neutrinos verifying such condition. To evaluate the real presence of a correlation between the two samples a background distribution called "semi-isotropic null" is constructed scrambling the RA values of UHECR events, keeping the Dec the same as in data. In this way we simulate on experiment, basing on the published PAO + TA data and on simulated (scrambled) ANTARES sample, in which only background and no signal is contained. We realized 10 000 simulations and each time the $\delta\chi_i^2$ distribution is added to the previous ones. At the end the average $\delta\chi_i^2$ distribution will represent the "null hypothesis".

For each simulation l we have N_{corr}^l events with $\delta\chi_i^2 \leq 1$, even if no signal is present. The distribution of N_{corr}^l will allow to evaluate the probability (p-value) to have a given N_{corr}^{exp} value by a background fluctuation. The p-value is calculated summing the number of times that N_{corr}^l of random sets is equal or exceeds the N_{corr}^{exp} of real data and dividing by the total number of data sets, that is 10 000.

In a second stage magnetic field effect is introduced. In particular the galactic backtracking changes the coordinates of particles according to simulations in par. 4.1.1. Deflection due to extragalactic field is inserted in the $\delta\chi_i^2$ formula in the

choice for the $\delta\gamma$, quadratically summed with the angular uncertainty of cosmic rays

$$\delta\theta^{new}_{\mathrm{UHECR}} = \sqrt{\delta\theta^2_{\mathrm{UHECR}} + \delta\theta^2_{def}} \tag{5.5}$$

where $\delta\theta_{def}$ is the matching deflection angle taken from simulations of par. 4.1.2. Then the same proceedings of the previous case is followed.

To understand the discovery potential of the analysis, we need to define the minimum number of "signal events" that can be statistically separated from the background. So we introduce average number of "good correlations" $< N^l_{corr} >$ that a background distribution can provide. The fluctuation of this number, calculated as the root mean square σ of N^l_{corr}, will define the minimum number of events that will allow a 1 σ, 3 σ and 5 σ discovery of a ν-CR correlation. For this scope a number k of fake signal events are injected in the background samples until $< N^l_{corr} > (k)$ exceed the value $< N_{hits} > +1$ σ, 3 σ and 5 σ. This gives us the number of N_{corr} needed to mimic a population that contains not only background events but also signals.

5.2.1 Considerations about the $\delta\chi^2$ values

We have performed a study about the possibility to use the $\delta\chi^2$ values, in order to define the "good matching" condition for a ν-UHECR common source. In particular, it is important to know the amount of signal events that could be excluded by the request $\delta\chi^2_i \leq 1$. To evaluate the fraction of signal with $\delta\chi^2_i \leq 1$ we have simulated the $\delta\chi^2$ distribution of signal events. Such a distribution can be obtained simulating neutrino events directly generated in the posistions indicated by PAO and TA as the UHECR origin. If we call $\mathcal{G}(0,1)$ a random value chosen from a Gaussian distribution with $mean = 0$ and $\sigma = 1$ we can construct fake neutrino signals taking the RA and Dec values of the cosmic rays, that here we call respectively α_{CR} and δ_{CR} and calculating:

$$\begin{cases} \alpha_\nu = \alpha_{CR} + \mathcal{G}(0,1) \cdot \sigma_{\alpha_{CR}} \\ \delta_\nu = \delta_{CR} + \mathcal{G}(0,1) \cdot \sigma_{\delta_{CR}} \end{cases} \tag{5.6}$$

where the two σ values are the uncertainties on the two cosmic ray coordinates taken directly from published data [29] [30]. These neutrino coordinates values are successively modified in a so-called "smearing", to take into account the uncertainty on the neutrino events, so we have

$$\begin{cases} \alpha^{new}_\nu = \alpha_\nu + \mathcal{G}(0,1) \cdot \sigma_{\alpha_\nu} \\ \delta^{new}_\nu = \delta_\nu + \mathcal{G}(0,1) \cdot \sigma_{\delta_\nu} \end{cases} \tag{5.7}$$

The values of σ_{α_ν} and σ_{δ_ν} are assumed to be the same for all neutrinos and we give them a value of $\sigma_{\alpha_\nu} = \sigma_{\delta_\nu} = 0.5^o$ [31]. We simulated 1000 events for each UHECR candidate source. then we eavluated the space angle between the fake neutrino events and the real UHECR and we obtained a $\delta\chi^2$ that represents the simulated signal-only distribution. In the two figs. 5.4 and 5.5 the $\delta\chi^2$ distributions for signal and background are compared. Form this distributions we can evaluate the amount

Figure 5.4. Distribution of $\delta\chi_i^2$ values for the case with no deflection. Blue filled plot is signal only distribution, Red lined plot is background only distribution.

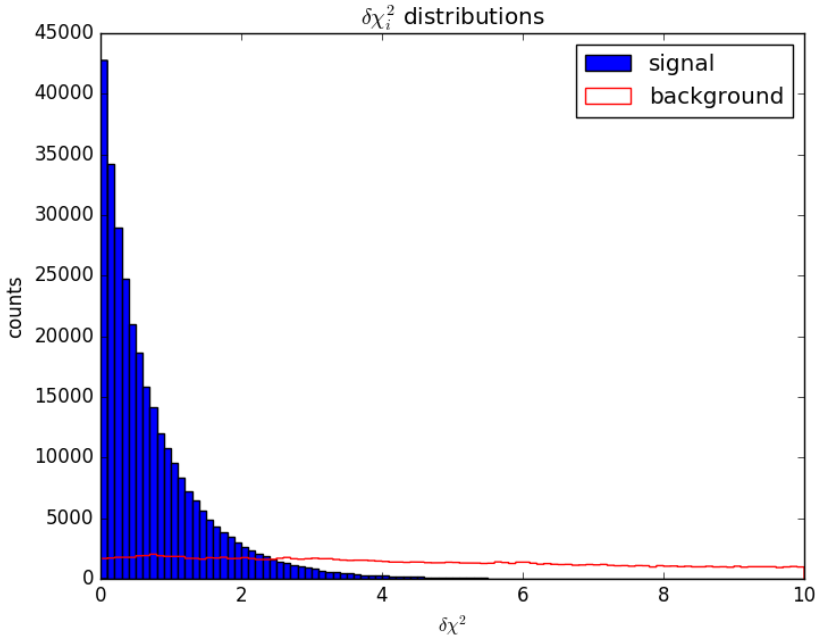

of signal and background events we include by considering the condition $\delta\chi_i^2 \leq 1$. Again we considered two cases:

1. the case in which deflection is neglected

2. the case in which deflection is taken into account as follows.

We assumed that UHECR are protons and that the mean deflection angle due to magnetic field is $\sim 3^o$. This choice is taken from the plot 4.4 looking a the proton (H) line at $\sim 50\,\text{EeV}$. Deflection angle $\delta\gamma_{def}$ is included in the formula for the $\delta\chi_i^2$ as

$$\delta\chi_i^2 = \min_j\left(\frac{\gamma_{ij}}{\delta\gamma_j + \delta\gamma_{def}}\right) \tag{5.8}$$

For the first case, in which we don't account for deflection due to the magnetic field, we show in fig. 5.4 the signal-only and background-only distributions. The horizontal axis is zoomed to display the region of major interest. The number of signal events with $\delta\chi_i^2 \leq 1$ is 74% of the total, that is more than those included in 1 σ (68%). The background events in the same $\delta\chi_i^2$ range is 6% of the total background events. In the second case, fig. 5.5 shows the histogram of the signal and background distributions for which the average magnetic deflection (3^o) was taken into account. In such case 63% of the signal distribution and 26% of the background events are within $\delta\chi_i^2 \leq 1$.

Figure 5.5. Distribution of $\delta\chi_i^2$ values for the case with deflection. Blue filled plot is signal only distribution, Red lined plot is background only distribution.

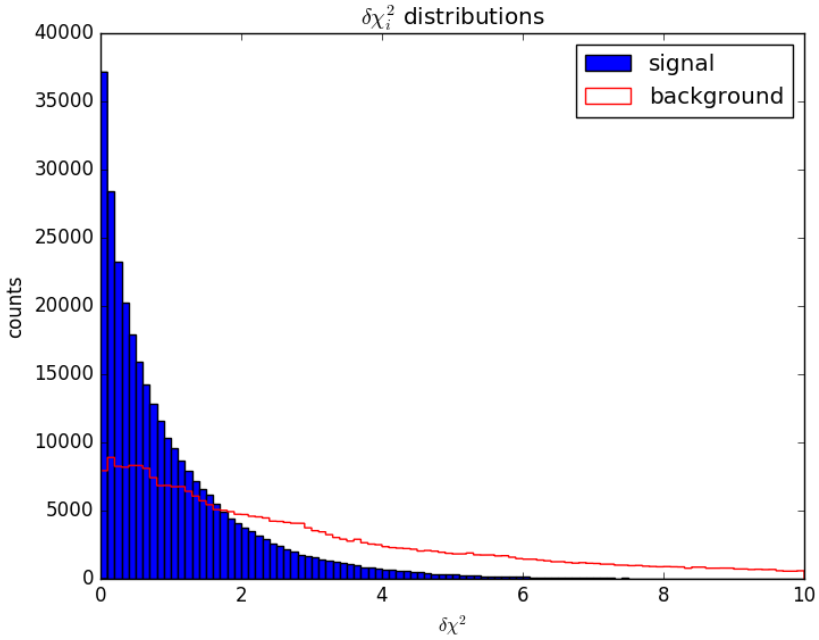

5.3 Analysis with IceCube neutrino events

5.3.1 Previous analysis results

As shown in [26], correlations were searched with different energy thresholds: $E > 100\,\mathrm{EeV}$ (32 events), 80 EeV (53 events) and 60 EeV (218 events). Two ways of simulating background data were used: in one the right ascension of cosmic ray data were randomized to construct a background and this is called "semi-isotropic null" distribution; in the other background is built randomizing declinations too and this is called "exposure-corrected null" distribution. In both cases 100 000 simulations of background were done and then the p-value was calculated comparing the number of good matches between background simulations and real data. Results of this analysis are showed in figs. 5.6, 5.7 and 5.8. As can be seen, the best p-values were found for cosmic rays with $E > 100\,\mathrm{EeV}$.

Figure 5.6. Values of $\delta\chi^2$ for cosmic ray events with $E > 100\,\mathrm{EeV}$. *Top left.* Data only from PAO. *Top right.* Data only from TA. *Bottom left.* Combined data from PAO and TA. *Bottom right.* Combined data from all experiments taken into account.

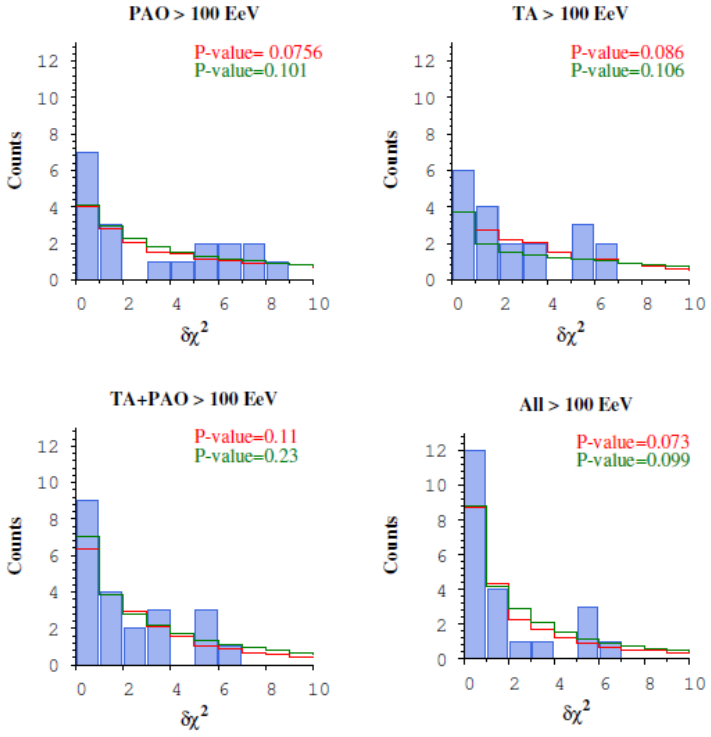

Figure 5.7. Values of $\delta\chi^2$ for cosmic ray events with $E > 80\,\mathrm{EeV}$. *Top left.* Data only from PAO. *Top right.* Data only from TA. *Bottom left.* Combined data from PAO and TA. *Bottom right.* Combined data from all experiments taken into account.

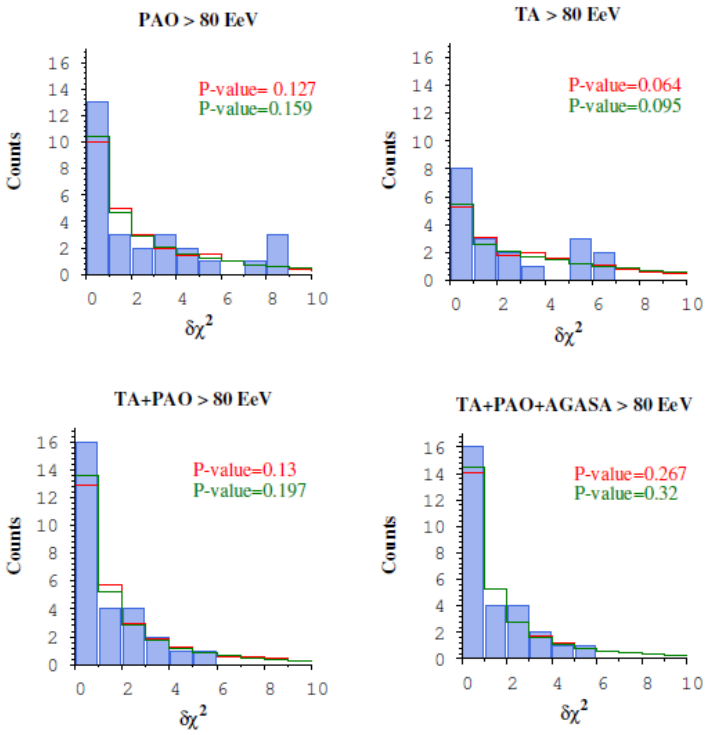

Figure 5.8. Values of $\delta\chi^2$ for cosmic ray events with $E > 60\,\mathrm{EeV}$. *Top left.* Data only from PAO. *Top right.* Data only from TA. *Bottom left.* Combined data from PAO and TA. *Bottom right.* Combined data from all experiments taken into account.

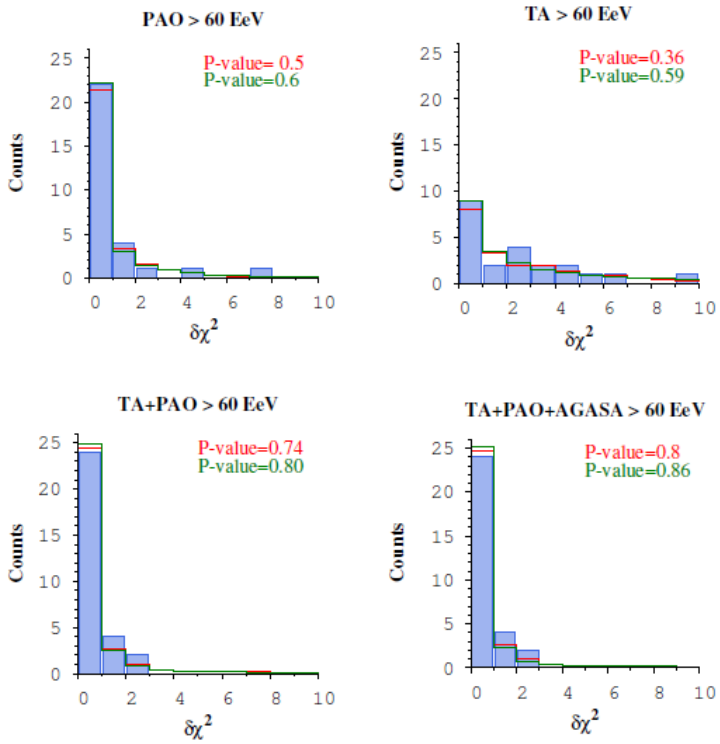

5.3.2 Test

To test the validity of our analysis method we have applied it to the sample of events published by IceCube and used in [26]. That have been used to obtain the results described in the previous paragraph. We considered the case with energy threshold $E > 100\,\mathrm{EeV}$. In fig. 5.9 there is the comparison of results. The exact matching between the Monte-Carlo simulated distributions indicates the success of the test.

Figure 5.9. *Up.* Results from [26]. *Down.* Our results. The red line is the semi-exposure null distribution in both plots.

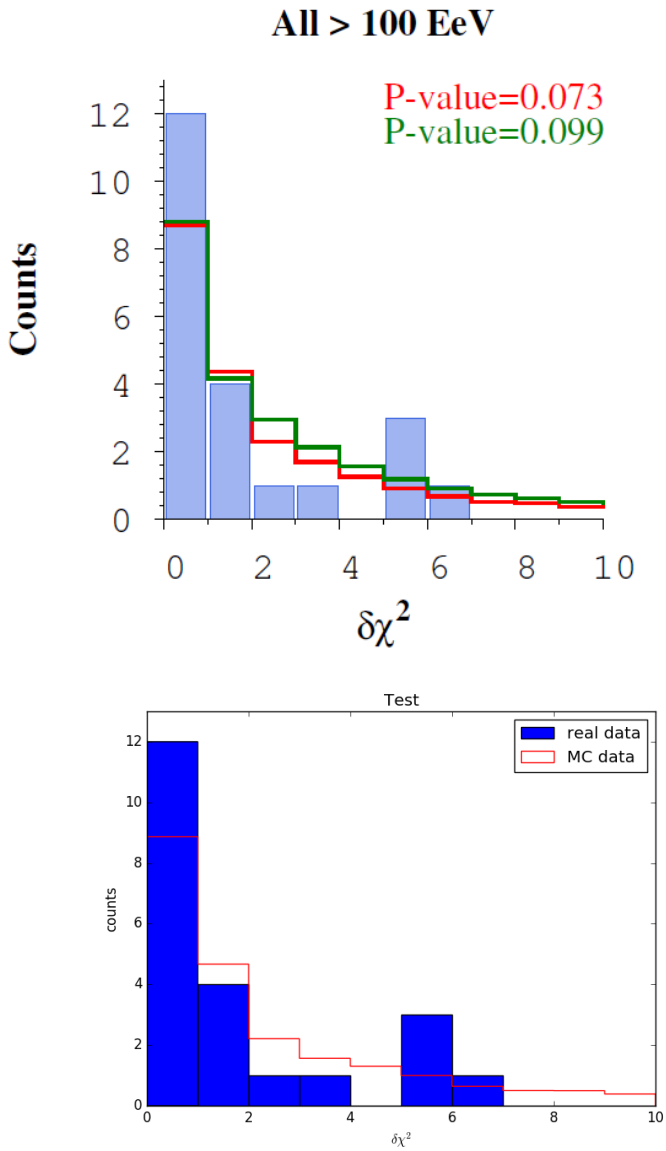

Chapter 6

Search for correlation between cosmic ray and neutrino events

We searched for the ν-CR correlation assuming two different hypotheses:

- the deflection of UHECR is neglected
- the UHECR are protons and their deflection in galactic and extragalactic path is taken into account

We will present in this chapter the results for both analysis. First the case without deflection is presented, then the case including magnetic field effect is discussed. The $\delta\chi_i^2$ distributions obtained for the background ("null hypothesis") and for the real neutrino and cosmic ray data are shown and compared.

6.1 No deflection case

The background distribution is calculated scrambling the RA of cosmic ray data and calculating for each neutrino i the $\delta\chi_i^2$ as function of the angular distance γ_{ij} between the neutrino and the cosmic rays and of the angular uncertainty is showed in the histogram in fig. 6.1 together with the distribution of $\delta\chi_i^2$ values distribution for real data. Number of events needed to emerge from background is reported. The number of counts in the first bin (that with the "good match") for null distribution is 10.93 and the 1σ value is 3.23, so 4 events are needed to exceed the $< N_{hits} > +1\sigma$ level, 11 events for the $< N_{corr} > +3\,\sigma$ level, 17 for the $< N_{corr} > +5\,\sigma$ level. The real data distribution has a N_{corr}^{exp} value of 10, well under the background mean level. The calculated p-value is $p = 0.659$, corresponding to more than 65% of the cases having a N_{corr} higher than that of real data.

6.2 Deflection included case

To take into account the UHECR deflection due to the magnetic field the choice of $\delta\gamma$ in the $\delta\chi^2$ formula in Equation 5.3 has been modified as follows

$$\delta\gamma = \max(\sqrt{\delta\theta^2_{\mathrm{UHECR}} + \delta\theta^2_{def}}, \delta\theta_\nu) \tag{6.1}$$

Figure 6.1. Results with no included deflection. p-value is showed and 1, 3 and 5 σ levels are marked.

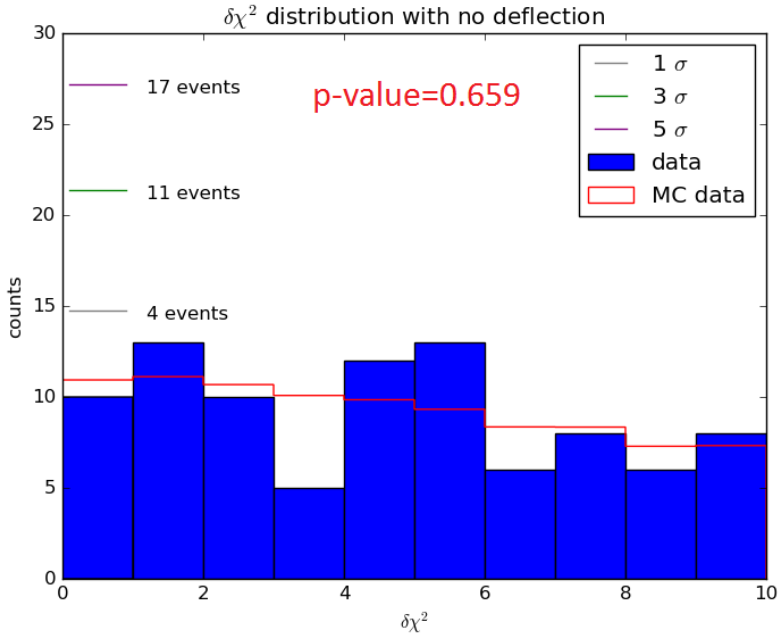

For this new case of interest, a new set of MC simulations has been generated to study the background. The results (fig. 6.2) show a $< N_{corr} >$ value of 16.11 with $1\,\sigma$ value being 3.82. In this case 5 events are needed to exceed the $< N_{corr} > +1\,\sigma$ level, 13 events for the $< N_{hits} > +3\,\sigma$ level, 21 for the $< N_{corr} > +5\,\sigma$ level. The deflected data distribution is shown in the same figure and has $N_{corr}^{exp} = 14$. Hence also for this case the data distribution is well compatible with a background distribution. The p-value calculated is $p = 0.742$, corresponding to 74.2% of the background simulated distributions having a higher N_{corr} than that of data.

Figure 6.2. Results including deflection. p-value is showed and 1, 3 and 5 σ levels are marked.

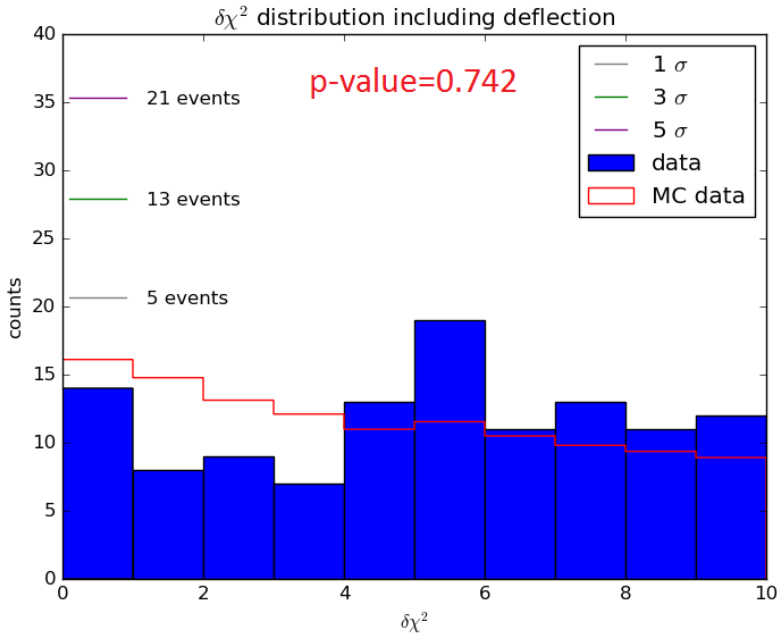

Chapter 7

Conclusion

In this work we wanted to perform a multimessenger study searching for correlation between public data of ultra high cosmic ray events recorded by the Pierre Auger Observatory and Telescope Array and neutrino track events by ANTARES. We presented cosmic rays as charged particles travelling in the Universe at high energies and neutrinos with all their very interesting characteristics such as low mass and low cross section. We also described the knowledges about galactic magnetic field (of the order of $\sim \mu$G) and extragalactic magnetic field (upper limits of the order of $\sim$ nG). We then presented the main experiments involved in detecting ultra high energy cosmic rays such as Pierre Auger Observatory, Telescope Array and other ones and detectors of high energy neutrinos such as ANTARES, IceCube and other ones. We also presented an overview on multimessenger astronomy displaying a few examples. We studied the influence on charged particles trajectories due to both galactic and extragalactic magnetic field with simulations using CrPropa finding some results:

- we evaluated the important galactic magnetic field contribution to deflection with an event by event analysis, finding an average deflection of $(4.66 \pm 3.28)^o$;
- we put rough limits on extragalactic deflection: we put an upper limit from Iron nuclei, having a deflection of the order of $\sim 10^o$ for $E > 50\,\text{EeV}$ in the case of a magnetic field with root mean square value of 1 nG; we set a lower limit from simulations of protons in the same magnetic field, being deflection $\lesssim 0.5^o$ for $E > 50\,\text{EeV}$;
- we found some interesting results about the free path length of atomic nuclei at ultra high energy, that seems to be correlated with the pair production energy threshold.

We perform a study on the distribution of $\delta\chi_i^2$ values, finding that for the case in which we do not account for deflection 75% of the signal events respect the chosen "good match" condition $\delta\chi_i^2 \leq 1$ and that for the case including deflection 63% of the signal distribution is within the chosen "good match" condition. Regarding the correlation between neutrino and cosmic ray events, the results we obtained show that there is no evidence for correlation between the two samples. In fact the number of events in the "good match" bin for the real data (N_{corr}^{exp}) is well describable

by a background-only distribution, being $N_{corr}^{exp} = 10$ and the $< N_{corr}^{k} > +1\ \sigma$ level at 15 for the case in which we do not account for deflection, and being $N_{corr}^{exp} = 14$ and the $< N_{corr}^{k} > +1\ \sigma$ level at 21 for the case in which we do consider deflection. The p-values calculated in each case confirm this, being both $p > 0.65$. We can be satisfied of the work done since we got very interesting results in the study of deflection due to galactic and extragalactic magnetic fields, and the finding of no correlation does not have to be considered a fail, but a motivation to go on with this kind of studies. We hope that deflection results will be useful in the future and that an extended study including ANTARES data after 2010 will be done, searching for common ν-UHECR point-like sources. Furthermore we hope that the continuous improvement of the detection instrumentation of present neutrino experiments such as IceCube and Baikal and the next starting of KM3Net and the develop of techniques of detection of cosmic rays, gravitational waves and high energy photons will take to important results in the search for sources and study the physical mechanisms involved with them (in particular those accelerating particles) and in the resolution of actual problems in cosmic ray spectrum and composition.

Appendix A

Tables of data

Details of data shown in graphics in chapter 4 and are presented here in tables.

A.1 Galactic deflection data

Here below is the table with data about deflection due to galactic magnetic field, already shown in map in subsection 4.1.1. The first three columns (E, RA_{obs}, Dec_{obs}) are the original values given by the PAO and TA experiments. The RA_{new} and Dec_{new} values are evaluated after deflection in galactic magnetic field with CrPropa, following the procedure described in subsection 4.1.1.

Table A.1

E[EeV]	RA$_{obs}$[deg]	dec$_{obs}$[deg]	RA$_{new}$[deg]	dec$_{new}$[deg]	unc[deg]
62.2	267.2	-11.4	277.6	-4.8	2.8
84.7	199.7	-34.9	199.4	-32.5	0.4
54.6	12.7	-56.6	16.9	-52.9	0.8
54.0	32.7	-85.0	37.1	-83.1	3.9
58.6	208.1	-60.1	211.2	-57.8	2.6
78.2	268.4	-61.0	274.3	-57.6	2.1
58.2	224.7	-44.0	228.8	-37.8	1.2
60.2	29.0	-14.0	32.3	-9.4	0.7
71.2	17.5	-37.8	20.9	-33.6	0.9
71.9	331.2	-1.3	332.0	4.7	1.0
52.1	199.1	-48.5	199.8	-45.9	1.9
108.2	45.6	-1.7	48.1	0.3	0.7
61.9	278.4	-1.3	285.8	3.0	2.5
54.9	333.0	-38.1	337.9	-30.3	0.9
74.9	114.8	-42.8	119.2	-40.5	1.0
77.5	18.3	29.2	21.3	34.2	0.8
78.2	18.9	-4.7	21.2	-0.8	0.6
72.2	53.6	-7.8	57.5	-4.3	1.0
52.8	267.6	-60.6	276.2	-56.4	2.9
64.8	275.2	-57.2	283.8	-51.4	2.0
69.5	201.1	-55.3	204.2	-54.0	1.8

Table A.1. Continued

E[EeV]	RA_{obs}[deg]	dec_{obs}[deg]	RA_{new}[deg]	dec_{new}[deg]	unc[deg]
54.7	28.8	-16.4	32.4	-11.8	1.0
56.3	322.5	-2.0	324.5	6.7	1.1
82.0	299.0	19.4	293.5	24.2	1.4
64.3	121.8	-52.5	127.3	-49.5	0.9
60.7	52.7	-43.4	55.9	-40.2	1.3
89.0	349.9	9.3	351.5	14.2	0.9
53.0	82.1	14.6	90.3	16.7	1.6
54.0	142.3	-13.1	143.6	-13.7	1.0
67.7	53.0	-4.5	56.7	-1.2	0.7
59.5	200.9	-45.3	202.3	-41.9	1.6
60.0	305.6	-46.3	312.3	-38.9	1.0
53.8	321.0	8.1	321.8	18.6	1.0
127.1	192.8	-21.2	191.7	-19.5	0.8
52.2	192.6	17.2	188.0	21.7	0.8
60.0	200.2	-43.4	200.6	-39.9	1.1
60.8	143.4	-18.1	144.6	-18.6	0.9
70.3	17.5	13.6	20.4	17.7	0.8
68.4	47.5	-12.8	51.5	-9.0	0.5
53.6	137.3	6.2	137.9	5.8	1.0
54.9	245.8	8.5	250.0	18.2	1.1
61.5	219.5	-53.9	224.4	-50.5	2.3
79.7	325.5	-33.4	329.3	-27.4	0.8
57.0	265.9	5.9	273.8	12.0	1.5
61.9	195.5	-63.4	200.9	-59.6	3.0
67.8	212.8	-3.1	210.9	1.6	0.7
60.7	192.5	-35.3	191.7	-32.0	0.5
68.1	185.3	-27.9	184.5	-26.2	0.4
60.8	105.9	-22.9	111.6	-19.2	2.0
65.9	325.7	-15.5	328.3	-8.0	1.3
55.8	39.2	19.4	43.9	24.2	0.6
52.5	59.6	38.3	66.4	43.1	2.0
54.0	250.3	1.8	256.0	11.6	1.0
82.4	81.6	-7.4	86.3	-5.4	0.7
72.7	315.3	-53.8	320.2	-48.9	1.4
80.2	271.1	19.0	276.1	22.9	1.0
64.2	252.7	-22.7	261.3	-11.2	2.0
111.8	352.6	-20.8	354.0	-18.0	0.6
65.3	187.5	-63.5	192.5	-60.8	2.8
60.4	19.8	-25.5	22.9	-22.2	0.7
56.0	64.1	-52.7	66.9	-49.9	1.2
53.3	202.0	-54.9	206.0	-53.2	2.1
56.2	82.8	-15.8	87.7	-13.0	0.8
52.4	184.4	-32.4	184.7	-29.5	0.6
73.1	220.6	-42.8	223.0	-38.1	1.6

Table A.1. Continued

E[EeV]	RA_{obs}[deg]	dec_{obs}[deg]	RA_{new}[deg]	dec_{new}[deg]	unc[deg]
62.9	110.2	-0.9	112.2	-1.0	1.5
56.7	199.4	6.6	195.8	10.9	0.8
55.7	33.0	11.0	37.5	15.8	0.8
55.1	306.5	-55.1	313.3	-49.3	0.8
56.7	358.9	15.5	2.3	22.4	1.1
52.0	67.7	4.0	73.8	9.0	1.1
89.3	116.0	-50.6	120.0	-48.9	1.2
61.2	339.4	-63.3	344.9	-59.9	1.0
118.3	287.7	1.5	283.9	7.0	0.9
58.1	202.2	-16.1	199.5	-12.7	0.8
64.7	15.6	-17.1	18.1	-12.9	0.7
62.2	25.0	-61.4	27.6	-58.2	1.1
63.1	126.4	5.3	126.4	4.8	0.9
66.9	28.9	-2.7	32.0	0.2	0.5
52.6	304.4	-26.2	306.5	-16.0	1.2
65.8	275.2	-14.4	279.2	-4.4	3.4
71.1	196.1	-69.7	201.0	-66.1	2.0
74.0	209.6	-31.3	208.8	-27.1	0.8
61.0	286.3	-37.8	292.5	-25.7	2.1
66.2	303.9	-16.5	305.2	-8.0	1.4
70.3	0.0	-15.4	2.2	-11.5	0.7
57.7	227.0	-85.2	233.4	-84.7	4.9
64.1	147.2	-18.3	148.0	-18.9	0.6
52.9	78.3	-16.0	84.6	-12.8	1.3
66.7	203.4	-33.0	202.1	-30.8	0.9
72.5	193.8	-36.4	192.8	-33.6	0.9
74.4	122.7	-54.7	128.0	-52.4	1.3
59.0	26.7	-29.1	29.5	-25.4	0.8
65.8	251.4	-35.8	258.7	-25.1	2.5
63.8	170.1	-27.4	170.7	-26.5	0.7
56.2	249.1	9.1	254.6	18.0	1.0
55.1	330.8	-8.9	333.8	-1.4	0.7
52.8	43.9	-25.4	47.2	-21.0	0.9
70.5	39.4	-34.5	42.1	-31.4	0.7
71.9	23.3	-40.2	25.8	-36.2	0.7
65.8	276.1	-33.4	280.1	-18.3	2.4
59.5	294.5	-20.5	295.6	-8.0	1.1
52.2	129.4	15.2	129.7	14.9	0.7
63.6	358.2	-2.8	1.1	2.3	0.9
55.3	122.5	-78.5	124.1	-77.2	2.4
53.2	29.4	-8.6	33.2	-3.5	0.6
58.3	304.3	-81.9	317.2	-81.8	4.2
70.0	325.8	42.8	319.5	48.8	2.3
52.3	212.7	29.9	210.3	37.4	0.5

Table A.1. Continued

E[EeV]	RA_{obs}[deg]	dec_{obs}[deg]	RA_{new}[deg]	dec_{new}[deg]	unc[deg]
58.7	50.1	-25.9	54.1	-21.8	0.4
82.3	287.7	-64.9	292.6	-62.4	1.0
75.3	256.7	14.0	261.9	19.5	1.2
60.8	47.6	11.5	51.9	15.0	1.0
58.6	217.9	-51.5	220.8	-48.9	2.6
55.6	177.7	-5.0	175.4	-2.6	0.7
52.5	171.3	-43.8	172.8	-42.9	1.1
54.3	97.2	34.3	100.7	34.5	1.7
61.5	174.7	-21.2	174.7	-19.6	0.4
64.5	227.9	-21.5	228.0	-15.0	0.8
72.9	258.1	-44.9	259.3	-33.3	2.9
66.9	278.8	7.9	285.8	8.9	1.6
82.0	122.7	-70.7	124.9	-69.7	1.5
74.8	89.2	-12.0	93.8	-9.4	1.2
54.7	197.8	-20.0	195.2	-16.1	0.7
58.4	149.2	5.5	149.3	5.3	0.7
53.8	277.2	6.7	288.7	9.4	2.0
52.3	303.7	-68.1	312.1	-65.0	1.4
53.2	180.5	-11.5	178.6	-8.8	0.3
53.5	315.8	-82.1	334.0	-81.4	5.0
56.1	250.2	-73.6	261.9	-72.0	3.7
65.2	284.7	-28.2	286.5	-15.5	1.8
75.6	324.5	17.9	324.6	24.8	0.9
60.3	216.1	-66.5	223.2	-65.6	2.5
69.6	226.4	-25.7	227.1	-20.2	0.9
58.4	312.9	-14.2	314.8	-5.1	1.1
76.1	131.9	-15.5	132.8	-15.7	0.6
73.7	12.3	-40.7	15.8	-37.1	0.6
89.1	218.8	-70.8	222.4	-68.0	2.4
58.0	8.4	-61.5	12.8	-58.1	0.9
53.1	118.1	8.5	119.0	8.5	0.7
70.5	64.2	-46.5	66.9	-44.2	1.0
55.0	118.6	-37.4	122.1	-35.4	1.9
54.3	80.2	-64.1	83.2	-62.1	0.9
68.7	121.1	-30.6	123.8	-30.1	2.8
54.6	170.9	-43.7	172.3	-42.9	1.1
54.9	231.9	-56.6	237.5	-51.1	3.3
54.4	179.7	-68.6	184.7	-62.6	1.7
68.0	167.0	-31.2	167.2	-30.2	1.1
69.4	268.5	-15.7	279.1	-9.7	2.1
100.1	150.1	-10.3	150.5	-10.3	0.7
54.0	185.4	-24.6	183.9	-22.0	0.6
58.2	33.4	-31.7	36.6	-28.3	0.9
52.0	125.5	-59.2	132.2	-56.3	1.3

Table A.1. Continued

E[EeV]	RA_{obs}[deg]	dec_{obs}[deg]	RA_{new}[deg]	dec_{new}[deg]	unc[deg]
62.7	215.5	-10.1	214.1	-4.8	1.0
60.3	239.4	3.9	242.4	12.7	0.9
71.1	230.3	1.5	231.2	9.5	0.4
56.2	160.3	-3.1	160.4	-2.7	0.7
81.4	308.8	16.1	306.3	22.8	1.1
69.7	30.3	3.8	34.0	7.9	0.8
54.8	295.1	-27.6	299.4	-16.0	1.9
67.3	255.4	-5.1	262.5	3.1	1.2
72.1	84.9	14.4	88.8	16.7	1.2
56.8	39.5	-29.9	43.1	-26.6	0.9
64.9	333.8	-79.2	344.4	-76.4	2.4
55.9	132.8	12.9	133.8	12.6	0.6
77.9	120.8	-56.3	124.8	-53.7	1.3
56.4	344.5	-19.9	347.2	-13.8	1.0
68.3	245.4	-18.2	250.4	-7.3	1.5
70.8	139.8	-35.8	141.3	-36.1	1.2
58.8	219.1	-41.9	219.9	-36.8	2.1
80.9	283.7	-28.6	285.1	-17.9	1.6
75.6	77.2	-41.0	80.9	-38.7	0.8
52.4	313.5	-16.6	315.2	-5.8	1.0
63.3	26.1	-32.2	28.7	-28.8	0.8
70.2	4.6	-37.9	7.9	-33.7	0.6
57.2	148.8	-13.0	149.1	-13.4	0.6
67.4	305.5	-34.5	310.2	-24.7	1.0
92.8	343.4	-71.6	347.8	-68.9	1.2
64.8	207.1	-29.1	206.2	-25.8	0.8
62.4	15.3	-3.6	19.1	1.4	0.9
66.1	33.2	-59.0	35.0	-56.4	1.1
99.0	309.4	-66.8	315.5	-64.6	1.5
70.4	154.0	-46.3	156.0	-46.3	0.9
62.6	37.8	-39.5	40.6	-35.4	0.6
58.5	189.0	-5.1	185.4	-2.1	0.7
58.7	37.0	-75.8	40.7	-74.0	2.3
60.0	245.4	-30.9	251.7	-20.9	2.0
83.8	26.8	-24.8	28.9	-22.0	0.6
61.8	259.8	-32.7	269.3	-20.9	2.7
61.1	18.7	-42.5	21.8	-37.9	0.8
54.4	342.9	-6.5	346.2	0.6	0.8
56.8	310.6	-83.1	325.9	-83.0	4.0
58.7	177.2	12.5	175.0	14.1	0.6
53.3	56.3	-3.2	60.9	0.6	0.8
71.1	227.6	11.9	228.8	18.2	0.6
55.7	217.1	-24.5	214.6	-19.4	0.8
62.7	200.9	-34.6	199.5	-31.6	0.6

Table A.1. Continued

E[EeV]	RA_{obs}[deg]	dec_{obs}[deg]	RA_{new}[deg]	dec_{new}[deg]	unc[deg]
70.7	56.6	-67.8	58.6	-66.7	1.3
53.2	314.9	-67.3	327.6	-62.5	1.1
73.6	267.5	-68.3	277.3	-66.3	1.9
71.9	73.7	-20.5	77.6	-18.3	1.1
53.9	154.3	-15.8	155.6	-15.6	0.9
62.1	138.6	26.1	137.9	25.6	0.9
57.3	357.0	-81.1	2.0	-79.1	1.6
85.3	123.4	-6.2	123.8	-7.1	0.6
54.3	33.3	-39.0	36.5	-34.9	0.7
52.2	0.4	-68.1	7.9	-63.6	0.9
58.9	211.1	15.0	209.0	20.9	0.6
68.8	64.7	-70.1	64.7	-68.8	1.0
67.3	308.1	-39.5	313.6	-31.8	0.8
61.5	240.3	-68.9	245.2	-66.1	2.0
63.4	345.4	-9.0	348.3	-3.0	0.8
84.8	154.6	-46.9	156.2	-46.6	0.7
55.5	160.4	-34.8	161.0	-34.6	1.2
65.4	92.1	-64.1	95.3	-62.1	1.1
58.5	327.5	-25.1	331.2	-17.4	0.9
73.0	163.8	-74.1	167.9	-72.9	2.2
54.6	298.7	8.8	294.0	19.1	1.6
54.4	284.5	-37.6	290.7	-22.9	1.9
52.9	286.8	-55.0	297.5	-49.6	1.2
63.6	182.3	-14.3	180.1	-12.0	1.0
65.2	241.6	-53.5	246.5	-43.5	3.4
72.5	91.4	-60.6	93.9	-59.4	1.2
53.2	198.8	-63.9	206.8	-58.8	3.4
60.0	72.8	-73.5	70.7	-72.3	1.1
74.5	189.9	-32.7	189.6	-31.0	0.9
54.6	186.7	-24.9	184.5	-22.3	0.9
54.9	2.3	-49.2	7.4	-44.5	1.0
60.2	239.5	-49.2	245.9	-39.8	2.8
63.6	45.2	-65.8	45.5	-63.2	1.6
118.3	340.6	12.0	341.1	15.9	0.7
88.8	93.5	20.8	94.0	21.9	1.8
82.6	68.9	19.2	73.1	22.4	2.0
101.4	285.7	-1.7	281.4	3.6	1.8
57.3	308.4	53.9	310.0	54.8	2.4
120.3	285.5	33.6	288.1	34.4	1.3
139.0	152.3	11.1	151.9	11.1	1.1
76.9	280.3	41.3	284.4	43.1	1.5
122.2	347.7	39.5	348.1	43.3	1.4
68.8	178.0	20.3	175.9	22.0	1.2
69.1	154.5	26.5	153.9	26.1	1.2

Table A.1. Continued

E[EeV]	RA_{obs}[deg]	dec_{obs}[deg]	RA_{new}[deg]	dec_{new}[deg]	unc[deg]
79.3	152.4	45.8	152.1	45.8	1.2
59.2	139.7	28.7	139.5	28.4	1.1
59.7	152.3	36.5	151.7	36.6	1.2
57.9	311.1	51.1	310.7	52.0	3.0
64.2	22.5	80.1	26.8	81.1	2.9
80.7	99.2	62.8	101.6	62.8	1.9
75.0	119.6	59.2	119.7	58.8	1.7
64.5	61.6	42.9	66.5	44.8	1.7
64.2	206.7	24.9	204.5	30.0	1.2
62.5	235.0	27.6	236.5	36.2	1.4
154.3	239.8	-0.4	241.5	3.2	1.2
59.5	305.1	44.4	304.9	46.1	3.0
65.2	331.6	18.9	332.0	26.3	1.2
61.7	56.5	64.4	61.3	66.6	4.5
66.5	82.2	43.1	85.9	43.6	1.8
64.0	120.0	46.0	119.8	45.5	1.3
57.6	128.8	44.5	129.2	44.0	1.4
61.2	78.8	61.4	80.1	61.5	2.3
63.7	139.1	49.6	139.1	48.8	1.0
65.2	25.3	44.0	29.6	49.9	2.0
58.0	212.4	-4.8	209.7	1.3	1.2
92.2	144.6	40.7	144.1	40.3	1.3
67.1	115.1	-1.4	116.3	-1.2	0.9
68.9	137.1	41.5	137.0	40.8	1.4
93.5	204.0	45.2	201.5	48.3	1.1
60.5	129.3	29.1	130.0	28.8	1.2
66.3	19.3	32.3	22.7	38.2	1.4
162.2	205.1	20.1	203.8	22.1	1.2
67.4	359.9	31.5	2.6	37.8	1.1
124.8	295.6	43.5	296.6	43.8	1.1
135.5	288.3	0.3	285.1	5.5	1.3
74.7	82.5	57.7	82.6	57.4	2.7
65.4	87.6	81.5	88.6	81.3	4.6
73.9	118.4	-1.4	118.8	-1.4	1.2
62.3	163.7	28.9	162.3	29.6	1.2
61.2	197.8	7.7	194.0	12.2	1.4
89.3	40.0	34.2	43.7	37.9	2.0
69.2	218.8	54.1	217.9	57.5	1.6
83.3	168.5	57.9	166.9	58.5	1.6
63.3	153.2	19.8	152.6	19.8	1.1
78.8	133.6	48.5	133.8	48.1	1.0
72.6	161.7	17.4	161.5	17.8	1.3
78.7	31.3	49.5	36.5	54.4	2.4
57.6	253.1	46.4	257.8	51.7	2.1

Table A.1. Continued

E[EeV]	RA_{obs}[deg]	dec_{obs}[deg]	RA_{new}[deg]	dec_{new}[deg]	unc[deg]
72.9	156.8	38.8	156.2	39.3	1.3
81.6	133.0	52.6	133.6	51.9	1.4
57.4	319.9	15.9	319.1	24.1	1.4
91.8	226.7	24.5	226.3	29.9	1.4
60.3	123.9	22.5	124.4	21.6	1.3
101.0	219.7	38.5	218.6	42.7	1.3
76.9	134.8	59.8	134.4	59.2	1.6
75.6	210.3	57.5	209.0	59.9	1.6
57.8	158.6	60.3	157.2	59.9	1.7
59.0	355.9	64.2	355.3	67.1	3.6
57.4	159.8	35.6	158.4	36.3	1.1
60.5	47.7	-4.7	51.6	-0.8	1.0
68.2	66.4	39.0	71.0	42.0	1.9
98.5	36.3	17.9	38.7	20.7	1.0
106.8	37.6	13.9	39.8	16.3	1.1
66.8	218.5	62.5	218.4	65.0	1.7
62.5	165.3	52.4	163.1	52.8	1.5
68.5	47.1	31.3	52.6	36.9	1.6

A.2 Extragalactic deflection data

Here are tables about deflection due to extragalactic magnetic field for different magnetic field intensities (MF1 and MF4 as defined in chapter 4). Data for protons and Iron are reported both with and without including interactions. For the second case tables for protons have the column with final energy E_{fin} and tables for Iron include the column "tr. length" indicating the free path length. Data for Helium, Oxygen, Silicon including interactions are reported even though they was not put in plots, including the column "tr. length" as for Iron.

Table A.2. Data for protons in MF1

	Interaction included			No interaction	
E[Eev]	defl[deg]	rms[deg]	Efin[EeV]	defl[deg]	rms[deg]
5	8.05	0.59	4.94	7.96	4.23
10	3.72	0.62	9.81	3.64	2.05
15	2.27	1.14	14.69	2.23	1.27
20	1.68	0.32	19.55	1.66	0.93
25	1.41	0.85	24.42	1.39	0.77
30	1.23	0.87	29.27	1.22	0.69
35	1.08	0.15	34.14	1.08	0.61
40	0.98	0.5	38.98	0.96	0.55
45	0.88	0.19	43.79	0.88	0.5
50	0.82	0.55	48.54	0.8	0.45
55	0.74	0.11	53.18	0.72	0.41

Table A.2. Continued

	Interaction			No interaction	
E[Eev]	defl[deg]	rms[deg]	Efin[EeV]	defl[deg]	rms[deg]
60	0.69	0.36	57.66	0.67	0.38
65	0.64	0.37	62.09	0.63	0.35
70	0.6	0.34	66.2	0.58	0.33
75	0.57	0.32	70.01	0.54	0.3
80	0.54	0.31	73.85	0.51	0.28
85	0.52	0.3	77.43	0.48	0.26
90	0.49	0.28	80.8	0.45	0.25
95	0.47	0.27	84.08	0.43	0.24
100	0.46	0.26	86.9	0.41	0.23
105	0.44	0.25	89.38	0.39	0.22
110	0.43	0.25	92.13	0.38	0.21
115	0.42	0.24	94.51	0.36	0.2
120	0.41	0.24	96.99	0.35	0.19
125	0.4	0.23	99.25	0.34	0.2
130	0.39	0.24	101.25	0.33	0.19
135	0.39	0.22	103.0	0.32	0.18
140	0.38	0.23	105.02	0.31	0.18
145	0.38	0.22	107.24	0.3	0.17
150	0.37	0.22	108.53	0.29	0.17
155	0.37	0.22	110.64	0.29	0.17
160	0.36	0.22	111.98	0.29	0.16
165	0.36	0.21	113.52	0.28	0.16
170	0.35	0.21	114.91	0.27	0.15

Table A.3. Data for Iron nuclei in MF1

	Interaction included			No interaction	
E[Eev]	defl[deg]	rms[deg]	tr. length[Mpc]	defl[deg]	rms[deg]
5	56.72	6.48	24.59	56.82	21.66
10	55.44	8.84	24.37	55.67	21.95
15	51.44	27.94	24.24	51.93	22.34
20	44.73	7.2	23.79	46.06	22.0
25	37.96	2.14	23.34	39.33	19.73
30	31.27	2.44	22.54	33.59	17.49
35	26.49	4.22	21.27	29.2	15.29
40	22.16	1.07	19.91	25.71	13.29
45	18.99	2.26	18.31	22.97	12.02
50	16.28	7.64	16.93	20.69	10.82
55	13.93	12.79	15.66	18.8	9.98
60	12.39	3.63	14.5	17.29	9.1
65	11.05	7.85	13.62	16.08	8.53
70	9.79	6.95	12.81	14.89	7.87
75	9.03	6.6	12.14	13.83	7.29

Table A.3. Continued

	Interaction included			No interaction	
E[Eev]	defl[deg]	rms[deg]	tr. length[Mpc]	defl[deg]	rms[deg]
80	8.07	6.02	11.58	13.08	6.95
85	7.59	5.69	11.3	12.25	6.39
90	6.98	5.23	10.93	11.65	6.09
95	6.46	4.9	10.57	10.89	5.7
100	6.12	4.7	10.29	10.48	5.56
105	5.71	4.44	9.91	9.89	5.26
110	5.44	4.21	9.83	9.47	5.0
115	5.16	4.04	9.58	9.06	4.81
120	4.82	3.78	9.19	8.66	4.59
125	4.57	3.57	9.1	8.36	4.39
130	4.32	3.47	8.87	8.05	4.25
135	4.07	3.3	8.54	7.74	4.14
140	3.83	3.1	8.15	7.43	3.95
145	3.54	2.9	7.71	7.1	3.81
150	3.37	2.81	7.37	6.84	3.67
155	3.16	2.59	6.91	6.6	3.57
160	2.88	2.41	6.38	6.42	3.45
165	2.67	2.25	5.81	6.28	3.37
170	2.44	2.07	5.34	5.96	3.26

Table A.4. Data for Helium nuclei in MF1

E[Eev]	defl[deg]	rms[deg]	tr. length[Mpc]
5	15.75	10.97	24.60
10	7.77	11.63	23.83
15	4.93	1.23	23.47
20	3.37	2.47	21.92
25	2.23	0.66	17.28
30	1.43	1.45	11.14
35	0.93	0.18	6.69
40	0.67	0.75	4.27
45	0.48	0.34	2.95
50	0.36	0.28	2.15
55	0.29	0.12	1.73
60	0.24	0.19	1.44
65	0.21	0.20	1.29
70	0.19	0.18	1.15
75	0.17	0.16	1.04
80	0.15	0.15	0.98
85	0.14	0.14	0.91
90	0.12	0.12	0.87
95	0.11	0.11	0.82
100	0.11	0.11	0.80

Table A.4. Continued

E[Eev]	defl[deg]	rms[deg]	tr. length[Mpc]
105	0.10	0.10	0.80
110	0.10	0.10	0.77
115	0.09	0.09	0.75
120	0.09	0.08	0.74
125	0.08	0.08	0.72
130	0.08	0.08	0.72
135	0.08	0.08	0.71
140	0.07	0.07	0.70
145	0.07	0.07	0.71
150	0.07	0.07	0.71
155	0.06	0.06	0.70
160	0.06	0.06	0.71
165	0.06	0.06	0.71
170	0.06	0.06	0.72

Table A.5. Data for Oxygen nuclei in MF1

E[Eev]	defl[deg]	rms[deg]	tr. length[Mpc]
5	50.38	24.36	24.71
10	30.61	20.0	24.2
15	20.02	1.88	22.8
20	14.52	4.20	21.11
25	11.09	7.30	19.93
30	9.01	1.24	19.16
35	7.50	3.62	18.31
40	6.42	2.63	17.55
45	5.48	2.36	16.68
50	4.65	3.85	15.35
55	3.88	3.05	13.49
60	3.17	0.56	11.27
65	2.53	2.02	8.75
70	1.94	1.58	6.41
75	1.53	1.27	4.83
80	1.22	1.05	3.54
85	0.99	0.87	2.65
90	0.83	0.74	2.08
95	0.67	0.62	1.62
100	0.56	0.54	1.30
105	0.48	0.48	1.07
110	0.43	0.43	0.93
115	0.37	0.37	0.81
120	0.32	0.33	0.67
125	0.29	0.30	0.61
130	0.27	0.27	0.53

Table A.5. Continued

E[Eev]	defl[deg]	rms[deg]	tr. length[Mpc]
135	0.24	0.25	0.48
140	0.21	0.22	0.43
145	0.20	0.21	0.39
150	0.18	0.19	0.37
155	0.17	0.18	0.34
160	0.16	0.16	0.32
165	0.15	0.16	0.30
170	0.14	0.14	0.28

Table A.6. Data for Silicon nuclei in MF1

E[Eev]	defl[deg]	rms[deg]	tr. length[Mpc]
5	55.63	13.77	24.73
10	47.52	10.28	24.51
15	34.76	16.82	24.01
20	26.21	18.26	22.87
25	20.05	10.85	21.3
30	16.00	29.23	19.58
35	13.16	14.22	18.34
40	11.21	4.22	17.38
45	9.67	1.56	16.41
50	8.51	1.62	15.95
55	7.67	3.02	15.47
65	6.23	4.35	14.76
70	5.70	4.02	14.25
75	5.21	3.75	13.77
80	4.84	3.49	13.32
85	4.20	3.18	12.08
90	3.72	2.86	10.96
95	3.32	2.66	9.8
100	2.78	2.28	8.16
105	2.42	1.99	6.89
110	2.05	1.77	5.72
115	1.74	1.50	4.61
120	1.46	1.27	3.56
125	1.25	1.10	2.86
130	1.07	0.96	2.37
135	0.92	0.83	1.93
140	0.80	0.76	1.62
145	0.70	0.68	1.36
150	0.62	0.59	1.17
155	0.55	0.55	1.02
160	0.49	0.49	0.88
165	0.44	0.45	0.77

Table A.6. Continued

E[Eev]	defl[deg]	rms[deg]	tr. length[Mpc]
170	0.41	0.41	0.69

Table A.7. Data for protons in MF4

	Interaction included			No interaction	
E[Eev]	defl[deg]	rms[deg]	Efin[EeV]	defl[deg]	rms[deg]
5	31.76	16.64	4.94	31.38	16.41
10	16.41	8.57	9.81	16.06	8.43
15	10.81	5.73	14.69	10.69	5.61
20	8.13	4.31	19.55	7.97	4.24
25	6.4	3.44	24.4	6.34	3.39
30	5.28	2.91	29.27	5.2	2.88
35	4.4	2.45	34.13	4.31	2.42
40	3.71	2.15	38.98	3.65	2.08
45	3.21	1.87	43.79	3.15	1.82
50	2.81	0.87	48.54	2.78	1.58
55	2.56	0.16	53.19	2.47	1.41
60	2.31	0.49	57.64	2.23	1.29
65	2.15	0.42	62.03	2.04	1.15
70	1.99	0.11	66.13	1.89	1.08
75	1.88	0.7	70.2	1.77	1.0
80	1.79	0.31	73.87	1.67	0.95
85	1.69	0.46	77.41	1.58	0.9
90	1.64	0.65	80.85	1.52	0.85
95	1.59	2.24	83.83	1.44	0.81
100	1.53	0.35	86.69	1.4	0.79
105	1.51	1.1	89.41	1.34	0.75
110	1.48	0.74	92.21	1.3	0.73
115	1.43	1.26	94.44	1.25	0.71
120	1.41	0.05	96.69	1.21	0.68
125	1.39	0.06	98.53	1.17	0.66
130	1.34	0.98	100.89	1.15	0.64
135	1.34	1.55	102.84	1.1	0.63
140	1.3	0.76	105.16	1.08	0.62
145	1.29	0.16	106.59	1.06	0.6
150	1.27	0.81	108.16	1.01	0.57
155	1.25	0.26	109.7	1.0	0.57
160	1.23	0.09	111.3	0.96	0.56
165	1.21	0.17	112.85	0.95	0.54
170	1.2	0.72	115.4	0.92	0.52

Table A.8. Data for Iron nuclei in MF4

	Interaction included			No interaction	
E[Eev]	defl[deg]	rms[deg]	tr. length[Mpc]	defl[deg]	rms[deg]
5	57.04	21.56	24.6	57.06	21.52
10	57.07	21.5	24.4	57.17	21.53
15	57.1	21.65	24.16	57.14	21.5
20	56.5	21.87	23.81	56.8	21.79
25	56.25	22.0	23.28	56.86	21.79
30	55.5	22.31	22.42	56.48	21.65
35	54.05	22.61	21.18	56.18	21.99
40	52.28	38.2	19.95	55.42	21.98
45	49.76	11.71	18.36	55.4	21.96
50	47.03	34.71	16.95	53.89	22.12
55	44.0	15.85	15.57	53.05	22.4
60	41.0	32.85	14.63	52.28	22.21
65	38.19	0.21	13.84	50.7	22.54
70	35.29	12.67	12.94	49.29	22.06
75	33.26	6.85	12.44	47.81	22.09
80	30.52	3.45	11.58	46.23	21.79
85	28.85	2.46	11.15	44.25	21.56
90	26.93	6.11	10.93	42.66	21.07
95	25.42	5.79	10.58	40.83	20.59
100	23.76	7.56	10.21	39.26	19.93
105	22.68	4.98	10.05	37.73	19.43
110	21.45	8.93	9.81	36.04	18.7
115	20.36	20.85	9.54	35.09	18.05
120	19.35	16.78	9.39	33.42	17.37
125	18.22	10.44	9.07	32.3	16.85
130	17.2	1.64	8.83	31.29	16.34
135	16.34	12.68	8.47	30.16	16.09
140	15.46	7.81	8.19	29.33	15.24
145	14.44	19.91	7.82	28.46	14.86
150	13.72	2.84	7.34	27.27	14.36
155	12.77	10.1	6.93	26.4	13.96
160	11.75	0.5	6.42	25.68	13.58
165	10.93	4.49	5.91	24.93	13.12
170	10.02	8.3	5.28	24.09	12.57

Table A.9. Data for Helium nuclei in MF4

E[Eev]	defl[deg]	rms[deg]	tr. length[Mpc]
5	50.16	22.50	24.62
10	30.40	16.41	23.85
15	20.57	11.26	23.44
20	14.90	8.63	21.91

Table A.9. Continued

E[Eev]	defl[deg]	rms[deg]	tr. length[Mpc]
25	10.23	6.63	17.44
30	6.56	4.98	11.23
35	4.11	3.32	6.71
40	2.81	2.13	4.15
45	2.06	2.93	2.96
50	1.57	0.92	2.20
55	1.25	0.96	1.78
60	1.02	0.72	1.47
65	0.86	0.76	1.29
70	0.77	0.65	1.17
75	0.65	0.34	1.02
80	0.58	0.65	0.95
85	0.54	0.44	0.92
90	0.49	0.38	0.85
95	0.46	0.46	0.83
100	0.42	0.43	0.78
105	0.40	0.24	0.77
110	0.38	0.09	0.75
115	0.36	0.03	0.75
120	0.35	0.03	0.74
125	0.33	0.37	0.74
130	0.31	0.07	0.72
135	0.30	0.06	0.71
140	0.28	0.14	0.71
145	0.28	0.12	0.72
150	0.27	0.26	0.71
155	0.26	0.36	0.72
160	0.25	0.09	0.70
165	0.24	0.06	0.70
170	0.24	0.24	0.71

Table A.10. Data for Oxygen nuclei in MF4

E[Eev]	defl[deg]	rms[deg]	tr. length[Mpc]
5	56.68	21.80	24.76
10	55.71	21.94	24.18
15	53.37	22.47	22.70
20	46.97	23.22	21.15
25	40.08	22.45	19.96
30	34.09	20.33	19.11
35	29.66	18.5	18.26
40	25.74	8.38	17.70
45	22.10	15.61	16.74
50	18.93	25.36	15.42

Table A.10. Continued

E[Eev]	defl[deg]	rms[deg]	tr. length[Mpc]
55	15.89	15.45	13.39
60	13.14	1.20	11.25
65	10.54	10.13	8.61
70	8.41	4.75	6.69
75	6.54	1.19	4.80
80	5.26	2.95	3.60
85	4.34	1.48	2.76
90	3.45	1.78	2.09
95	2.88	2.84	1.65
100	2.35	0.57	1.31
105	2.02	2.54	1.12
110	1.72	0.59	0.93
115	1.51	1.46	0.80
120	1.33	1.24	0.69
125	1.19	1.25	0.62
130	1.08	1.32	0.54
135	0.96	0.25	0.48
140	0.89	0.75	0.44
145	0.79	0.59	0.40
150	0.73	0.41	0.37
155	0.68	0.67	0.34
160	0.64	0.40	0.31
165	0.59	0.47	0.30
170	0.54	0.59	0.28

Table A.11. Data for Silicon nuclei in MF4

E[Eev]	defl[deg]	rms[deg]	tr. length[Mpc]
5	57.07	21.52	24.69
10	56.72	21.66	24.48
15	55.60	22.09	23.99
20	54.88	22.08	22.91
25	52.11	22.99	21.36
30	48.19	23.6	19.74
35	44.11	23.36	18.30
40	39.73	1.23	17.34
45	36.02	12.67	16.72
50	31.94	7.84	15.82
55	29.56	26.16	15.49
60	26.95	24.33	15.09
65	24.63	3.73	14.65
70	22.66	20.52	14.18
75	20.71	11.77	13.76
80	18.93	12.95	13.02

Table A.11. Continued

E[Eev]	defl[deg]	rms[deg]	tr. length[Mpc]
85	17.24	21.76	12.34
90	15.33	7.66	10.96
95	13.66	7.73	9.92
100	11.56	9.92	8.13
105	10.26	8.99	7.05
110	8.47	7.36	5.49
115	7.39	0.91	4.70
120	6.09	0.15	3.52
125	5.39	9.64	3.02
130	4.55	2.71	2.36
135	3.89	3.49	1.96
140	3.39	3.37	1.65
145	2.95	2.94	1.40
150	2.57	2.25	1.19
155	2.29	2.28	1.03
160	2.02	0.13	0.88
165	1.82	2.58	0.78
170	1.62	1.64	0.69

Bibliography

[1] M. Spurio. *Particles and Astrophysics*. Ed. by Springer. 2015.

[2] J.C. Arteaga-Velazquez and W.D. Apel et al. "The KASCADE-Grande experiment: measurements of the all-particle energy spectrum of cosmic rays". In: (2010).

[3] R. Adam and P. A. R. Ade et al. for Planck collaboration. "Planck intermediate results. XLII. Large-scale Galactic magnetic fields". In: *Astronomy & Astrophysics* (2016).

[4] R. Jansson and G. R. Farrar. "A new model for the Galactic Magnetic Field". In: *AP. J.* 757.1 (2012).

[5] M. S. Pshirkov, P. G. Tinyakov, and F. R. Urban. "New limits on extragalactic magnetic fields from rotation measures". In: *Phys. Rev. Lett.* 116 (2016).

[6] P.A. Cherenkov. "Visible Radiation Produced by Electrons Moving in a Medium with Velocities Exceeding that of Light". In: *Phys. Rev.* 52 (1937), pp. 378–379.

[7] K. Greisen. "End to the Cosmic-Ray Spectrum?" In: *Phys. Rev.* 16 (17 1966), pp. 748–750.

[8] G. T. Zatsepin and V. A. Kuz'min. "Upper Limit of the Spectrum of Cosmic Rays". In: *Journal of Experimental and Theoretical Physics Letters* 4 (1966), p. 78.

[9] M. Plum et al. for the Pierre Auger Collaboration. "Measurement of the chemical composition of the ultra-high-energy cosmic rays with the Pierre Auger Observatory". In: *arXiv:1501.06325v1* (2015).

[10] R.U. Abbasi and M. Abe et al. "Study of Ultra-High Energy Cosmic Ray Composition Using Telescope Array's Middle Drum Detector and Surface Array in Hybrid Mode". In: *Astropart.Phys.* 65 (2015), pp. 49–62.

[11] C. Kopper, N. Kurahashi, and N. Whitehom for IceCube collaboration. "Evidence for High-Energy Extraterrestrial Neutrinos at the IceCube Detector". In: *Science* 342 (2013).

[12] D. Semikoz. "High-energy astroparticle physics". In: *Proceedings, 5th CERN-Latin-American School* (2010).

[13] A. J. Heijboer. "Track Reconstruction and Point Source Searches with ANTARES". Ph.D. Thesis. Universiteit van Amsterdam, 2004.

[14] S. Adrian-Martinez and A. Albert et al. for the ANTARES collaboration. "A Search for Neutrino Emission from the Fermi Bubbles with the ANTARES Telescope". In: *Eur. Phys. J. C* (2014).

[15] *Pierre Auger Observatory*. URL: `https://www.auger.org`.

[16] E. L. Barcikowski. "The Composition of Ultra High Energy Cosmic Rays through Hybrid Analysis at Telescope Array". Ph.D. Thesis. The University of Utah, 2011.

[17] K. Weidenhaupt for the Pierre Auger Collaboration. "Radio Detection of Cosmic Rays at the Auger Engineering Radio Array". In: *Proceedings Of Science* 141 (2014).

[18] *Telescope Array*. The University of Utah. URL: `http://www.telescopearray.org`.

[19] R. Smida. "Cosmic-Ray Physics with the Pierre Auger Observatory". Ph.D. Thesis. Academy of Sciences of the Czech Republic, 2009.

[20] C. W. James. "Highlights from ANTARES, and prospects for KM3NeT". In: *The 34th International Cosmic Ray Conference* (2015).

[21] S. Adrian-Martinez. "Design and Development of an Acoustic Calibrator for Deep-Sea Neutrino Telescopes and First Search for Secluded Dark Matter with ANTARES". Ph.D. Thesis. Universitat Politecnica de Valencia, 2015.

[22] *IceCube*. University of Wisconsin-Madison. URL: `https://icecube.wisc.edu/`.

[23] S. Adrian-Martinez and A. Albert et al. for the ANTARES collaboration. "ANTARES constrains a blazar origin of two IceCube PeV neutrino events". In: *Astronomy & Astrophysics* 56 (2015), p. L8.

[24] M.G. Aartsen and M. Ackermann et al. "Multimessenger search for sources of Gravitational Waves and High-Energy Neutrinos: Results for the initial LIGO-Virgo and IceCube". In: *Phys. Rev.* 90.10 (2014).

[25] S. Adrian-Martinez and A. Albert et al. for the ANTARES collaboration. "High-energy Neutrino follow-up search of Gravitational Wave Event GW150914 with ANTARES and IceCube". In: *Phys. Rev.* 93.12 (2016).

[26] R. Moharana and S. Razzaque. "Angular correlation of cosmic neutrinos with ultrahigh-energy cosmic rays and implications for their sources". In: *JCAP* (2015).

[27] S. Adrian-Martinez and A. Albert et al. for the ANTARES collaboration. "First combined search for neutrino point-sources in the Southern Hemisphere with the ANTARES and IceCube neutrino telescopes". In: *Ap. J.* 823.1 (2016).

[28] R. Alves Batista and M. Erdmann et al. "CRPropa: a public framework to propagate UHECRs in the universe". In: *JCAP* (2016).

[29] A. Aab and P. Abreu et al. for the Pierre Auger collaboration. "Searches for Anisotropies in the Arrival Directions of the Highest Energy Cosmic Rays Detected by the Pierre Auger Observatory". In: *Ap.J.* 804.1 (2015).

[30] R. U. Abbasi and M. Abe et al. for Telescope Array collaboration. "Indications of Intermediate-scale Anisotropy of Cosmic Rays with Energy Greater Than 57 EeV in the Northern Sky Measured with the Surface Detector of the Telescope Array Experiment". In: *The Ap. J. Lett.* 790.2 (2014), p. L21.

[31] T. Montaruli for the ANTARES collaboration. "Search for Cosmic Neutrino Point Sources with four Years of Data from the ANTARES Telescope". In: *Ap.J.* 760.53 (2012).